NATIONAL TECHNICAL UNIVERSITY OF ATHENS
School of Naval Architecture and Marine Engineering
Division of Ship and Marine Hydrodynamics

A Semi-Lagrangian Splitting scheme for the free surface Euler system with application to rotational wave flows in general bathymetry

---

Andreas Alexandris-Galanopoulos

A diploma thesis presented for the degree of
integrated Master of Engineering

Supervisor: K.A. Belibassakis, Professor
Committee members: L. Kaiktsis, Professor
G. Papadakis, Assistant Professor

Athens, Greece
February 27, 2023

Abstract

In the present thesis, a numerical scheme for the Free-Surface Euler system in general bathymetry is presented. The σ-coordinate is generalized in a layer-wise manner and the Generalized-Coordinate Euler system (GCE) is proposed. The system is treated by a standard operator splitting technique with the addition of a layer kinematic scheme.

As a result, the GCE is split into the Multilayer Shallow Water Equations (mSWE), followed by the proposed Vertical Remeshing Operator (VRO) and the standard Pressure Correction Operator (PCO). Those three operators constitute the Semi-Lagrangian Splitting scheme (SLS).

The mSWE and VRO are solved by two separate Finite Volume schemes. The PCO is solved by a partially implicit approach, followed by the solution of a Poisson-like equation on a staggered grid through a Finite Difference method.

The SLS's performance is tested on the wave propagation over variable bathymetry and wave-current interaction over a flat bottom cases.

Acknowledgements

This thesis marks the end of my studies at the National Technical University of Athens and as such, I feel the need to mention some people that played a key role during those years.

First and foremost, I must wholeheartedly thank my supervisor, Professor K.A. Belibassakis for introducing me to the field of ocean and marine hydrodynamics and proposing the extremely interesting *rotational flows* as the subject of the thesis. His input and support throughout the stages of the present thesis kept me focused and helped in sparking a profound interest in research.

My gratitude also extends to Professors G. Papadakis and G.A. Athanassoulis for also shaping my academic background. Various conversations with the former helped in introducing me into the field of CFD, while the latter influenced through his courses the way I approach mathematical modeling. I thank them both.

On a more personal note, I would like to thank my colleagues Aggelos, Pavlos, Sifis and Spyros. Throughout my studies, interacting and sharing experiences with them shaped me in a profound personal (and academic) level. Same thanks are owed to my family. I wish them the best.

Last, but not least, I would like to thank Areti. During the majority of my time at NTUA, she has been by my side in a way that truly redefines the meaning of companionship. I thank her for the endless support and apologize for the (also endless) amount of proofreading I have put her through.

Contents

1 Introduction **9**

1.1 Motivation 9

1.2 Approaches to mathematical modeling 10

1.3 Main framework and scope of the thesis 11

1.4 Thesis outline 12

2 The Free-Surface Euler system **14**

2.1 Description in cartesian coordinates 15

2.2 Vertical coordinate systems 17

2.2.1 z-models (Cartesian frame) 17

2.2.2 ρ-models (Lagrangian frame) 18

2.2.3 σ-models (Terrain following) 18

2.3 The σ-coordinate system 19

2.3.1 Tranformation of operators 20

2.3.2 The Sigma-Coordinate Euler system 21

3 The Semi-Lagrangian Splitting scheme **22**

3.1 Hybrid coordinate methods 22

3.2 The layerwise Generalized-Coordinate Euler system 23

3.2.1 Getting the SCE from the GCE 25

3.2.2 Variable reconfiguration 26

3.3 Layer kinematics . . . 28
3.4 The operator splitting formulation . . . 29
3.5 Discretization of variables . . . 30
3.6 The discrete Semi-Lagrangian Splitting scheme . . . 32

4 The Multilayer Shallow Water Equations 33
4.1 The Shallow Water Equations solver . . . 34
4.1.1 Eigenstructure of the SWE . . . 35
4.1.2 The finite volume scheme . . . 36
4.1.3 Roe's Riemann solver . . . 36
4.1.4 Second order reconstruction and slope limiters . . . 38
4.1.5 Hydrostatic reconstruction and source term . . . 40
4.1.6 Boundary conditions and timestepping . . . 42
4.2 The uncoupled mSWE scheme . . . 46

5 The Vertical Remeshing Operator 48
5.1 Remeshing and kinematic considerations . . . 49
5.2 Spatial resolution . . . 50
5.2.1 Flux reconstruction . . . 50
5.2.2 Boundary conditions . . . 51
5.3 Temporal resolution and final scheme . . . 52

6 The Pressure Correction Operator 54
6.1 The partially implicit approach . . . 54
6.2 Grid staggering . . . 56
6.3 Discrete equations and boundary conditions . . . 57
6.4 Variable and gradient reconstruction . . . 60
6.5 The PCO algorithm . . . 61

7 The SLS as a numerical wave tank **64**

7.1 Boundary conditions and relaxation zones 64

7.2 Stability and timestepping scheme 66

7.3 Dispersion properties and wave/current propagation 69

7.3.1 Irrotational waves 69

7.3.2 Current incorporation and boundary data 70

8 Numerical results **73**

8.1 Propagation over submerged trapezoid 73

8.2 Wave-current interaction 76

9 Concluding remarks **79**

9.1 Brief summary 79

9.2 Directions for future research 80

A Generalized Vertical Coordinates **81**

B The two-layer SWE **83**

C Discrete dispersion relation **85**

List of Figures

1.1 The physical problem 9
1.2 Structure of the proposed model 12

2.1 The free surface setup 14
2.2 Vertical coordinate systems 17
2.3 The σ-coordinate transformation 19

3.1 Sample layer configuration for $N_l = 5$ 24
3.2 The layer kinematic scheme 28
3.3 Variable indexing on the 2D mesh 31

4.1 SWE variable reconstruction 40

5.1 VRO variable reconstruction 51

6.1 Grid staggering technique 58

7.1 Generation/ absorption zones 65
7.2 Dispersion relation curves 72
7.3 Celerity error curves 72

8.1 The immersed trapezoid setup 73
8.2 Submerged trapezoid, P field 74

8.3 Submerged trapezoid, Q field 74
8.4 Submerged trapezoid, q field 75
8.5 Free surface elevation at stations 75
8.6 No current 77
8.7 Linear current profile 77
8.8 Exponential current profile 78

B.1 The two-layer SWE 83

List of Algorithms

1 SWE variable reconstruction 44
2 SWE residual calculation 45
3 Multilayer Shallow Water Equations solver 47
4 Discrete VRO scheme 53
5 The PCO reconstruction scheme 62
6 Discrete PCO scheme 63
7 The discrete SLS 68

Acronyms

CFD Computational Fluid Dynamics. 1, 11, 57

FSE Free-Surface Euler system. 1, 2, 10–12, 14–18, 20, 22, 23, 25, 79, 82

GCE Generalized-Coordinate Euler system. 1, 2, 12, 13, 23, 25, 27, 28, 79, 82

mSWE Multilayer Shallow Water Equations. 1, 3, 7, 12, 13, 32–34, 46, 47, 49, 50, 64, 66–68, 79, 83

PCO Pressure Correction Operator. 1, 3, 7, 12, 13, 32, 54, 60–64, 66–68, 79, 85

SCE Sigma-Coordinate Euler system. 2, 21, 25, 82

SLS Semi-Lagrangian Splitting scheme. 1, 3, 7, 13, 22, 29, 32, 64, 66, 68, 69, 76, 78–80, 85

SWE Shallow Water Equations. 3, 5, 12, 13, 34, 35, 37, 40, 42, 46, 47, 80

VLR Vertical Lagrangian Remapping. 23, 29

VRO Vertical Remeshing Operator. 1, 7, 12, 13, 32, 46, 48–53, 56, 64, 67, 68, 79

Chapter 1

Introduction

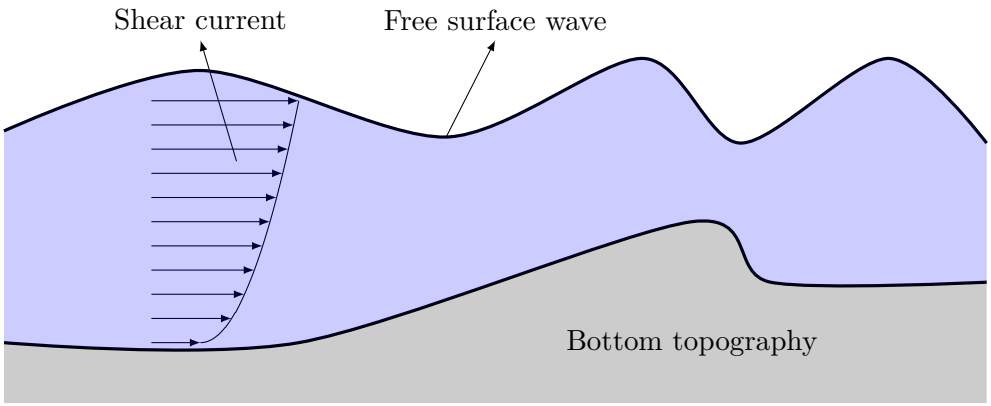

Figure 1.1: The physical problem

1.1 Motivation

In coastal areas, water flows are often dominated by the presence of strong currents and steep bathymetries. At the same time, free surface waves and their interaction with human-made structures is of great importance for safety and engineering purposes. As such, the development of efficient numerical models that accurately capture those phenomena is highly motivated. Among the difficulties in the description of such models is the inclusion of complex interactions (wave-bottom,wave-current) that are inherently nonlinear and often of multi-scale nature. Because of those complications, great care must be given in order to strike a balance between the model's ability to describe those phenomena and

its computational efficiency.

Specifically, it has been recently established that the presence of a shear currents greatly influences the propagation of free-surface waves [1, 2] and thus, suitable numerical models for the simulation of wave-current interaction have been proposed [3]. Under the assumption of constant shear (linear current profile), extended mild slope [4, 5] and couple mode [6] models have been proposed and experimentally validated [7]. Extensions of the couple mode system for the case of waves propagating in the presence of currents with general vertical profiles have also been proposed [8, 9].

In the present work, a more direct approach is adopted. The standard Euler equations describing the motion of an incompressible fluid of constant density are directly discretized and a numerical model able to simulate rotational flows of arbitrary nature is obtained. The model's only main restriction is that both the free surface and bottom topography boundaries are considered to be single valued functions of the horizontal coordinate. This system is referred to as the Free-Surface Euler system (FSE) and will be the starting point of the present approach.

1.2 Approaches to mathematical modeling

When constructing a numerical method for a physical problem, two approaches appear to be prevalent. The first one is to propose a mathematical model that is tailor made to capture the physics of the problem and then propose a suitable discretization based on that. The second one is to choose a more universal numerical method and then apply it to the problem at hand with some minuscule problem-specific modifications.

While the former approach ensures that all the relevant quantities are modeled and handled properly, the proposed numerical method is often not optimal due its case-specific construction.

On the other hand, the adoption of a more universal method comes with a high base quality, because established methods become over time more robust and computationally efficient due to the accumulated amount of research. The main deficit of the second approach is that choosing the proper numerical method from a finite set of popularized ones means that its application on a specific problem may require some modifications. That can either alter its performance (stability, efficiency) or worsen its ability to capture the underlying physics.

Regarding the free surface water flows, those two different approaches are easily identified.

The first one consists of a series of mathematical models whose complexity ranges from

the Shallow Water Equations [10] and the Boussinesq-type models [11, 12, 13] to more complex formulations that are able to describe flows with arbitrary vertical structure [14, 15]. Those models are designed to maximize their capability to capture the physics with careful mathematical modeling, while lowering the complexity (or size) of the variables/operators in use. The numerical resolution of these methods, though, is often times suboptimal due to the fact that the unique form of those equations poses additional difficulties on the discretization.

The other approach falls within the general framework of the Computational Fluid Dynamics (CFD). Based on that, one chooses to solve a specific set of field equations that describe the fluid motion on a specific level of complexity. Common methods include Laplace, the Euler and the Navier-Stokes equations. Those equations are ubiquitous in the CFD community and thus standard numerical methods (Finite Elements, Finite Volume, Spectral, Particle methods e.t.c.) can be employed to solve them.

The main feature that is unique to the problem at hand is the incorporation of the free surface. One category of methods are the free surface capturing ones: the Volume of Fluid method (VoF) [16], the Level Set method [17] and the Marker-and-Cell method (MAC) [18]. Other approaches include the so called mesh-moving methods, either in the Arbitrary Lagrangian Eulerian (ALE) framework [19] or using the well known in the oceanographic community σ-coordinate system[1] [21].

Having said that, it is the firm belief of the author that between those two approaches exists a significant unexplored design space of methods that may prove to be highly effective. Bearing that in mind, the general strategy and scope of the thesis will be presented in the next sections.

1.3 Main framework and scope of the thesis

As it was briefly expressed in §1.1, the main goal of the thesis is to propose a numerical method for the Free-Surface Euler system, able to capture rotational phenomena of oceanographic interest. After the brief description of §1.2 regarding the already existing approaches to the free surface problem, the adopted approach/framework is left to be specified.

For the purposes of the present work, the splitting strategy is employed, where a complicated problem (or operator) is divided into a set of sub-problems that are easier to handle. An ubiquitous example from CFD is the projection method of Chorin [22], where the incompressible Navier-Stokes operator is splitted into the advection+diffusion part and the pressure+divergence free one. The last one is transformed into a Poisson

[1] For the connection between those two approaches see [20].

equation, which is heavily analysed both in the theoretical and numerical aspect. That kind of approach generally gives rise to schemes with block structure that are easier to analyse, build and maintain because their components (if chosen carefully) are of interdisciplinary nature and thus are heavily supported by the bibliography. This serves as the main inspiration for the proposed numerical method.

Due to the aforementioned advantages, the main scope of the thesis is to present a splitting scheme for the Free-Surface Euler system that correctly captures both the velocity field and free surface kinematics in a straightforward and mathematically consistent manner. When possible, the mathematical modeling is done in a way so that the fundamental building blocks of the proposed method are either present in the literature or straightforward in their description.

Following the discussion of §1.2 the splitting scheme is designed so that one of the resulting subsystems coincides with an already existent simplified free surface model, which as will be illustrated in the maid body of thesis, is the classic Shallow Water Equations (SWE). That ensures a seamless incorporation of the free surface kinematics into the solver and combines the approaches mentioned in §1.2.

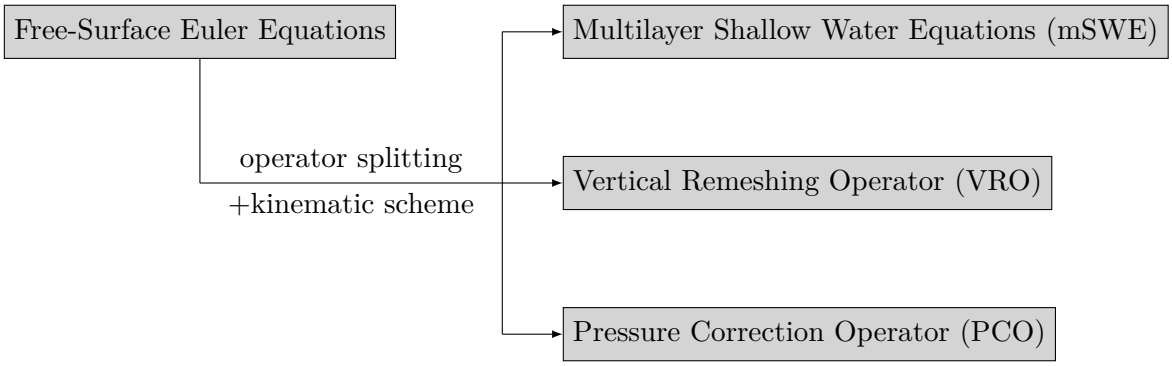

Figure 1.2: Structure of the proposed model

1.4 Thesis outline

The thesis is structured as follows:

In Chapter 2 the Free-Surface Euler system (FSE) is presented and various vertical coordinate systems are described. The σ-coordinate counterpart of the FSE is generated.

In Chapter 3 the novel scheme for the FSE is proposed: The σ-coordinate transformation is generalized in a layer-wise manner and the Generalized-Coordinate Euler system

(GCE) is generated. Using an operator splitting technique combined with a layer kinematic scheme, the Semi-Lagrangian Splitting scheme (SLS) is proposed. The SLS consists of 3 basic operators: the Multilayer Shallow Water Equations (mSWE), the Vertical Remeshing Operator (VRO) and the Pressure Correction Operator (PCO). Those operators are separately described in their corresponding chapters that follow.

In Chapter 4 the numerical scheme for the first operator, the mSWE is described. The proposed discretization is based on the consecutive solution of a set of regular Shallow Water Equations (SWE). Because of that, a second-order Finite Volume solver for the SWE is described in detail, followed by its multilayer extension.

In Chapter 5 the VRO scheme is described. The remeshing technique and its discretization by a simple one-speed Finite Volume solver are presented.

In Chapter 6 the PCO is solved. The role of the operator is discussed and the numerical approach for its solution (partial implicit formulation, grid staggering, finite difference scheme) is described.

In Chapter 7 the use of the SLS as a numerical wave tank is presented. Relaxation zone techniques are discussed and the fully discrete time-marching scheme is formed. Discrete dispersion relations are presented and the properties of the scheme are analyzed.

In Chapter 8 the SLS is tested in both the propagation over general bathymetry and in the wave-current interaction cases.

In Chapter 9 conclusions and directions for future research are discussed.

Chapter 2

The Free-Surface Euler system

In the present chapter the Free-Surface Euler system (FSE) is described. The equations of motion are first presented in the cartesian frame and then other coordinate systems are discussed, focusing on the ubiquitous in oceanography σ-coordinate transformation.

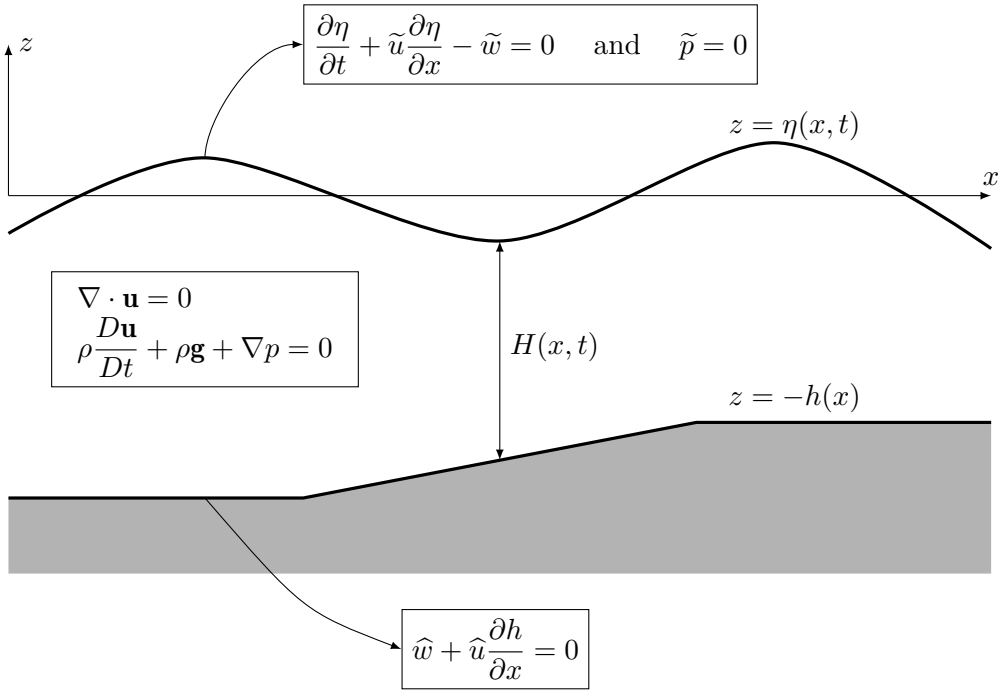

Figure 2.1: The free surface setup

2.1 Description in cartesian coordinates

As mentioned, we focus on the motion of a homogeneous fluid of constant density ρ that is vertically bounded by the bottom, $z = -h(x)$ and the free surface, $z = \eta(x,t)$. Those surfaces alongside the (cartesian) coordinate system can be seen in Fig.2.1. An important restriction that is imposed on that configuration is the positivity of the water column height: $H \overset{\text{def}}{=\!=} \eta + h \geq 0$.

If the viscosity effects are neglected, the flow in the domain can be described by the Euler equations:

$$\frac{\partial u}{\partial x} + \frac{\partial w}{\partial z} = 0 \tag{2.1a}$$

$$\frac{\partial u}{\partial t} + u\frac{\partial u}{\partial x} + w\frac{\partial u}{\partial z} + \frac{1}{\rho}\frac{\partial p}{\partial x} = 0 \tag{2.1b}$$

$$\frac{\partial w}{\partial t} + u\frac{\partial w}{\partial x} + w\frac{\partial w}{\partial z} + \frac{1}{\rho}\frac{\partial p}{\partial z} + g = 0 \tag{2.1c}$$

where u, w are the horizontal and vertical components of the velocity, p is the pressure and g is the gravitational constant.

The system is then complete with the addition of the kinematic and dynamic free surface boundary conditions:

$$\frac{\partial \eta}{\partial t} + \widetilde{u}\frac{\partial \eta}{\partial x} - \widetilde{w} = 0 \tag{2.2}$$

$$\widetilde{p} = 0 \tag{2.3}$$

and the bottom no-through boundary condition:

$$\widehat{u}\frac{\partial h}{\partial x} + \widehat{w} = 0 \tag{2.4}$$

Where $\widetilde{(\cdot)} = [(\cdot)]_{z=\eta}$ and $\widehat{(\cdot)} = [(\cdot)]_{z=-h}$ are the free surface and the bottom trace operators.

By defining the dynamic pressure as $q \overset{\text{def}}{=\!=} \frac{p}{\rho} - g(\eta - z)$ the Free-Surface Euler system

(FSE) is generated:

$$\frac{\partial u}{\partial x} + \frac{\partial w}{\partial z} = 0 \tag{2.5a}$$

$$\frac{Du}{Dt} + \frac{\partial q}{\partial x} + g\frac{\partial \eta}{\partial x} = 0 \tag{2.5b}$$

$$\frac{Dw}{Dt} + \frac{\partial q}{\partial z} = 0 \tag{2.5c}$$

$$\text{BC:} \quad \widetilde{q} = 0 \tag{2.5d}$$

$$\frac{\partial \eta}{\partial t} + \widetilde{u}\frac{\partial \eta}{\partial x} - \widetilde{w} = 0 \tag{2.5e}$$

$$\widehat{u}\frac{\partial h}{\partial x} + \widehat{w} = 0 \tag{2.5f}$$

with the material derivative defined as: $\dfrac{D(\cdot)}{Dt} \stackrel{\text{def}}{=\!=} \dfrac{\partial}{\partial t}(\cdot) + u\dfrac{\partial}{\partial x}(\cdot) + w\dfrac{\partial}{\partial z}(\cdot)$

Note that in the FSE described above, the fluid motion is completely contained between two boundaries (the free surface and the bottom) that are considered to be singled valued functions of the horizontal coordinate x. From a physical point of view, that assumption renders the description of overturning/breaking waves impossible, but greatly simplifies the model. In order to model such complex phenomena, one must employ the two-phase CFD methodologies that were mentioned in §1.2.

In the present model, no such method is used and thus the fluid is considered to be totally contained within a vertically compact (albeit moving and deforming) domain. This enables the design of methods for the vertical resolution of the system that adequetely incorporate the implicit character of the domain. An overview of those methods is presented in the next section.

2.2 Vertical coordinate systems

An apparent difficulty of the FSE (and the free surface models in general) is the fact that the equations describing the motion of the fluid are defined in a moving and deforming domain. Since the two boundaries (i.e. the free surface and the bottom) bound the fluid across the vertical axis, the coordinate system used for that direction plays an important role in the numerical scheme that will be employed.

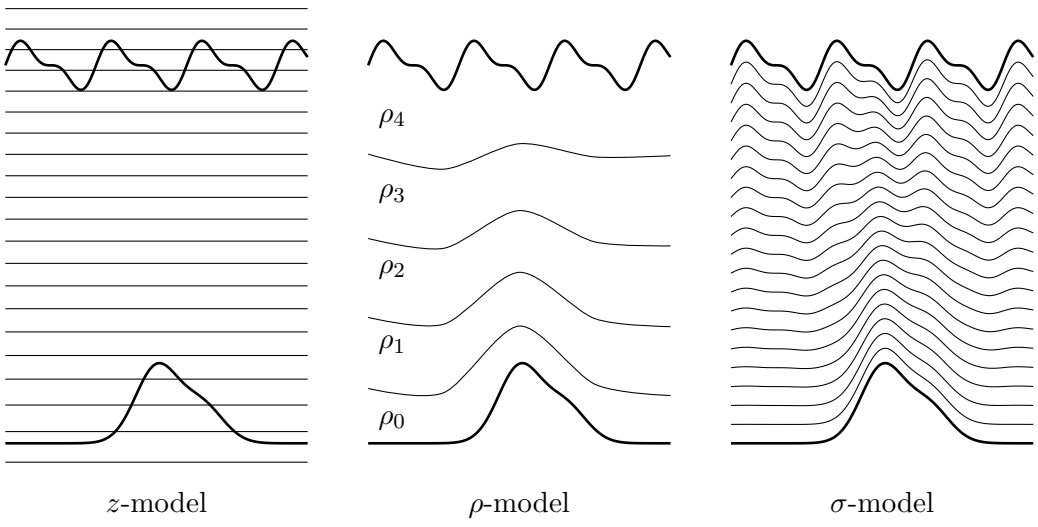

Figure 2.2: Vertical coordinate systems

Following [23], the three main vertical coordinate systems that are used within the oceanographic community are briefly described. Those systems fall within the Generalized Vertical Coordinate (GVC) framework introduced by Starr [24]. A GVC-like method for the FSE is also presented in Appendix A.

2.2.1 z-models (Cartesian frame)

Popularized by the work of Bryan [25] and used most notably in the GFDL Modular Ocean Model (MOM) [26], the use of Cartesian coordinates has been proven robust and efficient due to the natural discretization of state equations and easy grid structure.

The incorporation, though, of the free surface and bottom topography can be quite cumbersome because those surfaces intersect the cartesian grid and special care must be taken when the discretization near them is performed (see e.g. [27]).

2.2.2 ρ-models (Lagrangian frame)

In the so-called isopycnal models, the domain is split into horizontal layers, so that the fluid density is constant within each of them. This means that mixing between the layers is prohibited and thus the layer interfaces are forced to move in a Lagrangian way. Notable contributions to isopycnal models include the works of Hallberg [28] and Bleck [29].

This coordinate system is boundary-fitted and the advection of tracers can easily be incorporated due to the Lagrangian nature of the layers. The main disadvantage, though, derives from the fact that the isopycnal interfaces are of an arbitrary shape and thus discretization of equations (and gradients) can be rather difficult if large deformations occur.

2.2.3 σ-models (Terrain following)

Pioneered by Phillips [21], the σ coordinate is introduced so that the the water column is mapped on a fixed interval (usually $[-h, \eta] \mapsto [0, 1]$, using the notation of Fig.2.1). The most well-known oceanographic application of this method is in the Princeton Ocean Model (POM) [30].

Due to their terrain-following nature, the σ-models incorporate the boundaries in an analytic way and thus are ideal for coastal and engineering applications. Regarding the method's disadvantages, problems may arise in the numerical scheme as a consequence of the curvilinear nature of the coordinates. A classic example of that is the well-known problem in the evaluation of the horizontal pressure gradient [31].

Because the scheme proposed herein can be seen as a generalization of the σ-coordinate method, its application on the FSE will be presented in the next section.

2.3 The σ-coordinate system

The standard σ-coordinate transformation is given by:

$$(x, z, t) \longmapsto (x', z', t') \qquad \text{with:} \qquad \left\{ \begin{aligned} x' &= x \\ \sigma &= \sigma(x, z, t) = \frac{z + h(x)}{H(x, t)} \\ t' &= t \end{aligned} \right\} \tag{2.6}$$

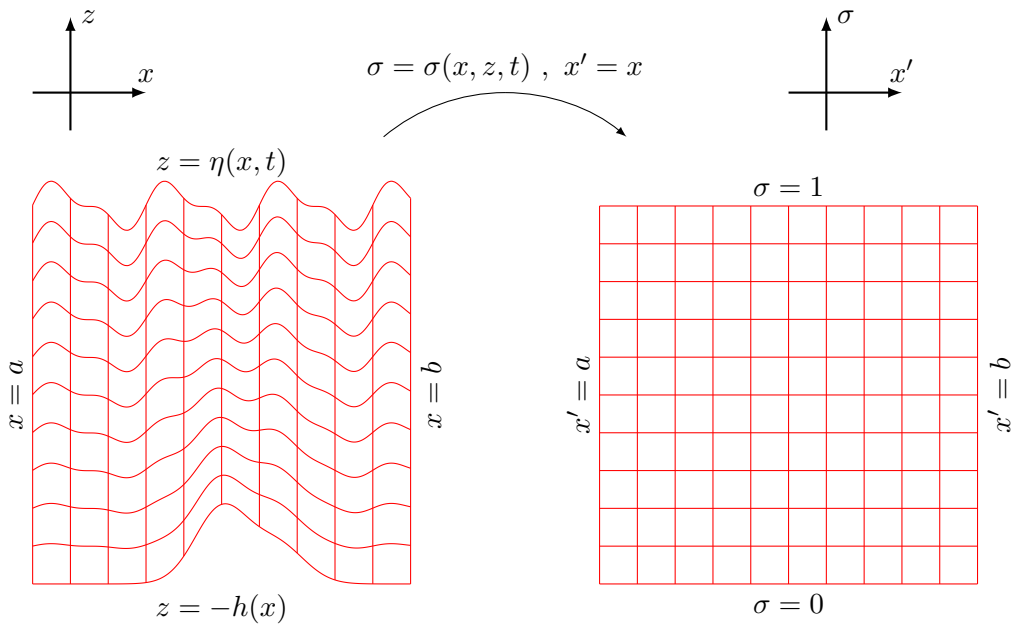

Figure 2.3: The σ-coordinate transformation

Based on that, the derivatives are transformed through the chain rule:

$$\frac{\partial}{\partial x} = \frac{\partial \sigma}{\partial x} \cdot \frac{\partial}{\partial \sigma} + \frac{\partial}{\partial x'} \tag{2.7a}$$

$$\frac{\partial}{\partial z} = \frac{\partial \sigma}{\partial z} \cdot \frac{\partial}{\partial \sigma} \tag{2.7b}$$

$$\frac{\partial}{\partial t} = \frac{\partial \sigma}{\partial t} \cdot \frac{\partial}{\partial \sigma} + \frac{\partial}{\partial t'} \tag{2.7c}$$

$$\frac{D}{Dt} = \frac{\partial}{\partial t'} + u \frac{\partial}{\partial x'} + \frac{D\sigma}{Dt} \cdot \frac{\partial}{\partial \sigma} \tag{2.7d}$$

Based on that, the derivatives of the iso-σ surfaces are defined as:

$$S_t \overset{\text{def}}{=\!=} H\frac{\partial \sigma}{\partial t} = -\sigma\frac{\partial H}{\partial t} \tag{2.8a}$$

$$S_x \overset{\text{def}}{=\!=} H\frac{\partial \sigma}{\partial x} = \frac{\partial h}{\partial x} - \sigma\frac{\partial H}{\partial x} \tag{2.8b}$$

$$S_z \overset{\text{def}}{=\!=} H\frac{\partial \sigma}{\partial z} = 1 \tag{2.8c}$$

Using the above, the "conservative" form of the partial derivatives is:

$$H\frac{\partial f}{\partial t} = H\frac{\partial f}{\partial t'} + S_t\frac{\partial f}{\partial \sigma} = \frac{\partial}{\partial t'}(Hf) + \frac{\partial}{\partial \sigma}(S_t f) - \cancel{f\left(\frac{\partial S_t}{\partial \sigma} + \frac{\partial H}{\partial t}\right)} \tag{2.9a}$$

$$H\frac{\partial f}{\partial x} = H\frac{\partial f}{\partial x'} + S_x\frac{\partial f}{\partial \sigma} = \frac{\partial}{\partial x'}(Hf) + \frac{\partial}{\partial \sigma}(S_x f) - \cancel{f\left(\frac{\partial S_x}{\partial \sigma} + \frac{\partial H}{\partial x}\right)} \tag{2.9b}$$

$$H\frac{\partial f}{\partial z} = \frac{\partial f}{\partial \sigma} \tag{2.9c}$$

The last two terms are zero by the definition of eq.(2.8) and thus the material derivative is written as:

$$\begin{aligned} H\frac{Df}{Dt} &= H\frac{\partial}{\partial t}(f) + H\frac{\partial}{\partial x}(uf) + H\frac{\partial}{\partial z}(wf) = \\ &= \frac{\partial}{\partial t'}(Hf) + \frac{\partial}{\partial x'}(Huf) + \frac{\partial}{\partial \sigma}(\varpi f) \end{aligned} \tag{2.10}$$

Where ϖ is defined by:

$$\varpi \overset{\text{def}}{=\!=} H\frac{D\sigma}{Dt} = S_t + uS_x + wS_z \tag{2.11}$$

The ϖ essentially represents the velocity component that is normal to the iso-σ surfaces. Note that this velocity is relative to the motion of said surfaces (incorporated through the term S_t).

2.3.1 Tranformation of operators

Returning to the FSE, its σ-coordinate is presented.

- The differential operators are transformed by directly applying eq.(2.9),(2.10).
  - The continuity equation:

$$H\left(\frac{\partial u}{\partial x} + \frac{\partial w}{\partial z}\right) = 0 \Rightarrow \frac{\partial}{\partial x'}(Hu) + \frac{\partial}{\partial \sigma}(uS_x + w) = 0 \tag{2.12}$$

– The horizontal momentum equation:

$$H\frac{Du}{Dt} + H\frac{\partial q}{\partial x} + gH\frac{\partial \eta}{\partial x} = 0 \Rightarrow$$
$$\Rightarrow \frac{\partial}{\partial t'}(Hu) + \frac{\partial}{\partial x'}\left(Hu^2 + \frac{1}{2}gH^2 + Hq\right) + \frac{\partial}{\partial \sigma}\left(\varpi u + S_x q\right) = \frac{\partial h}{\partial x}gH \tag{2.13}$$

– The vertical momentum equation:

$$H\frac{Dw}{Dt} + H\frac{\partial q}{\partial z} = 0 \Rightarrow \frac{\partial}{\partial t'}(Hw) + \frac{\partial}{\partial x'}\left(Huw\right) + \frac{\partial}{\partial \sigma}\left(\varpi w + q\right) = 0 \tag{2.14}$$

- The boundary conditions' structure is kept unchanged, but they are written in a more convenient manner.

  – The free surface dynamic condition stays the same: $\widetilde{q} = 0$

  – The kinematic conditions are expressed through the use of the velocity ϖ, thus further reinforcing its physical meaning:

$$\widetilde{\varpi} = \widetilde{w} - \frac{\partial \eta}{\partial t} - \widetilde{u}\frac{\partial \eta}{\partial x} = 0 \tag{2.15}$$
$$\widehat{\varpi} = \widehat{u}\frac{\partial h}{\partial x} + \widehat{w} = 0 \tag{2.16}$$

2.3.2 The Sigma-Coordinate Euler system

Summarizing those results, the Sigma-Coordinate Euler system (SCE) in the domain $(x', \sigma) \in \mathbb{R} \times [0, 1]$ is presented:

$$\frac{\partial}{\partial x'}(Hu) + \frac{\partial}{\partial \sigma}\left(w + uS_x\right) = 0 \tag{2.17a}$$
$$\frac{\partial}{\partial t'}(Hu) + \frac{\partial}{\partial x'}\left(Hu^2 + \frac{1}{2}gH^2 + Hq\right) + \frac{\partial}{\partial \sigma}\left(\varpi u + S_x q\right) = gH\frac{\partial h}{\partial x} \tag{2.17b}$$
$$\frac{\partial}{\partial t'}(Hw) + \frac{\partial}{\partial x'}\left(Huw\right) + \frac{\partial}{\partial \sigma}\left(\varpi w + q\right) = 0 \tag{2.17c}$$
$$\text{BC: } \widetilde{\varpi} = \widehat{\varpi} = \widetilde{q} = 0 \tag{2.17d}$$

Chapter 3

The Semi-Lagrangian Splitting scheme

In the present chapter, the mathematical formulation of the proposed Semi-Lagrangian Splitting scheme (SLS) for the FSE is presented. Since the SLS falls within the broad family of Hybrid-coordinate / Vertical Lagrangian Remap methods that are used within the oceanography community, the relevant existing literature is briefly overviewed. After that, and following the framework of Generalized Vertical Coordinates (GVC), the σ-coordinate is generalized in a layerwise mannner. The resulting system, combined with a layer kinematic scheme, is treated through an operator splitting and, finally, the continuous and discrete forms of the SLS are presented.

3.1 Hybrid coordinate methods

As it was described in §2.2, the three main Generalized Vertical Coordinates (GVC) each have their corresponding advantages and drawbacks and thus the choice between them is not always an obvious one. For example, if one decides to use the ρ-model because of its natural advection of tracers and ability to simulate internal waves, the isopycnal layers are forced to move in a Lagrangian manner. Even though this may prove to be an excellent choice for most of the domain, there may areas where large deformations or singularities occur. Those problems are easily overcome if another GVC is used in those regions. In that case, one would like to adopt a hybrid approach that switches between the basic GVC systems based on the corresponding flow configuration.

This lead to the introduction of a hybrid ρ/z-model by Bleck [32], where if a layer's thickness approaches zero, a remeshing technique on the fixed z-grid is performed and thus

the layers are redefined. This Vertical Lagrangian Remapping (VLR) technique has been used with success in the HYCOM [33] and the MOM6 [34] ocean models and has inspired a wide class of methods like the frequency-filtering ALE schemes of [35] and [36]. For an extensive (and recent) review of the VLR methods in use for oceanographic applications, we refer to [37].

Even though the majority of the VLR methods have been applied to hydrostatic models, a small number of schemes have also been constructed for models free of that assumption. Those include the atmospheric models of [38] and [39] and the multilayer approach of [40]. The last one bears a lot of similarities regarding the structure of the operator-splitting scheme (Multilayer SWE + remapping + Projection step) used in the method proposed herein, but the derivation and numerical solution of those operators differ in a significant way.

A VLR-like technique for the FSE will be presented in then next sections.

3.2 The layerwise Generalized-Coordinate Euler system

Consider a set of functions $\{z_j(x,t)\}_{j=0}^{j=N_l}$ that produce a layer-like partition of the water column as follows:

$$-h(x) = z_0(x,t) \leq \cdots \leq z_j(x,t) \leq \cdots \leq z_{N_l}(x,t) = \eta(x,t) \tag{3.1}$$

Now, consider a set of constant in space and time numbers $\{\xi_j\}_{j=0}^{j=N_l}$ that form a tessellation of the interval $[0,1]$:

$$0 = \xi_0 \leq \cdots \leq \xi_j \leq \cdots \leq \xi_{N_l} = 1 \tag{3.2}$$

Based on those, the quantities $\{L_j\}_{j=0}^{j=N_l-1}$ can be defined as:

$$L_j(x,t) \stackrel{\text{def}}{=\!=} \frac{z_{j+1} - z_j}{\xi_{j+1} - \xi_j} = \frac{\Delta z_j}{l_j} \tag{3.3}$$

$$\text{with: } l_j \stackrel{\text{def}}{=\!=} \xi_{j+1} - \xi_j \tag{3.4}$$

Note that by definition of the ξ_j, the l_j form a partition of unity: $\sum l_j = 1$. The quantities L_j play an important role in the present layerwise approach and will be referred to as the *layer indicators*.

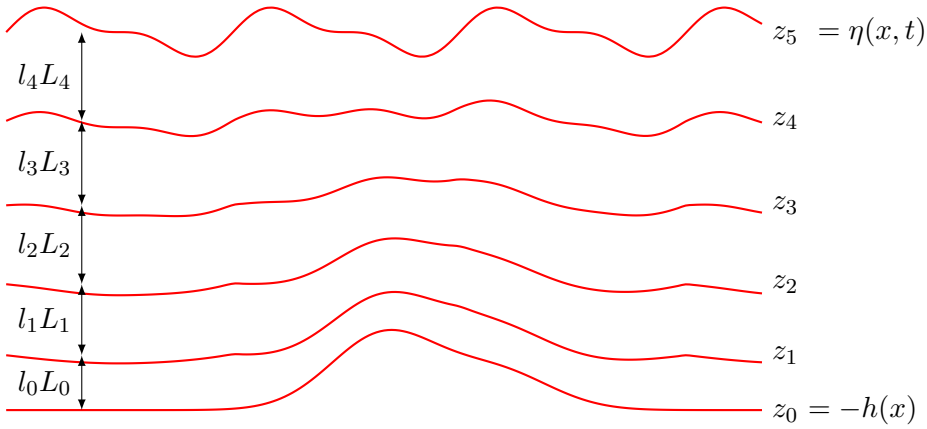

Figure 3.1: Sample layer configuration for $N_l = 5$

Now, let us consider a smooth mapping that interpolates those layer interfaces:

$$(x', \xi, t') \longmapsto (x, z, t) \quad \text{with:} \quad \left\{ \begin{matrix} x = x' \\ z = \mathcal{P}_\Xi(x', \xi, t') \\ t = t' \end{matrix} \right\} \tag{3.5}$$

$$\text{so that:} \quad \mathcal{P}_\Xi(x', \xi_j, t') = z_j(x', t') \qquad , \quad j = 0, ..., N_l - 1 \tag{3.6}$$

In order to transform the derivatives, we define (see Appendix A):

$$L \overset{\text{def}}{=\!=} \frac{\partial \mathcal{P}_\Xi}{\partial \xi} \tag{3.7a}$$

$$\Xi_t \overset{\text{def}}{=\!=} -\frac{\partial \mathcal{P}_\Xi}{\partial t'} \tag{3.7b}$$

$$\Xi_x \overset{\text{def}}{=\!=} -\frac{\partial \mathcal{P}_\Xi}{\partial x'} \tag{3.7c}$$

Note that the layer indicators are related to the quantities $L(x', \xi, t')$ through:

$$L_j \overset{(3.3)}{=\!=} \frac{\Delta z_j}{l_j} \overset{(3.7a)}{=\!=} \frac{1}{l_j} \int_{\xi_j}^{\xi_{j+1}} L d\xi \tag{3.8}$$

Following the analysis of Appendix A, the derivatives are transformed:

$$L\frac{\partial f}{\partial t} = L\frac{\partial f}{\partial t'} + \Xi_t \frac{\partial f}{\partial \xi} = \frac{\partial}{\partial t'}(Lf) + \frac{\partial}{\partial \xi}(\Xi_t f) \tag{3.9a}$$

$$L\frac{\partial f}{\partial x} = L\frac{\partial f}{\partial x'} + \Xi_x \frac{\partial f}{\partial \xi} = \frac{\partial}{\partial x'}(Lf) + \frac{\partial}{\partial \xi}(\Xi_x f) \tag{3.9b}$$

$$L\frac{\partial f}{\partial z} = \frac{\partial f}{\partial \xi} \tag{3.9c}$$

and then similarly:

$$\begin{aligned} L\frac{Df}{Dt} &= L\frac{\partial}{\partial t}(f) + L\frac{\partial}{\partial x}(uf) + L\frac{\partial}{\partial z}(wf) = \\ &= \frac{\partial}{\partial t'}(Lf) + \frac{\partial}{\partial x'}(Luf) + \frac{\partial}{\partial \xi}(\vartheta f) \end{aligned} \tag{3.10}$$

with the velocity that is normal the the coordinate lines being:

$$\vartheta \overset{\text{def}}{=\!=} w + u\Xi_x + \Xi_t \tag{3.11}$$

Note that the role of ϑ is essentially the same as that of ϖ in the σ-coordinate transformation.

Thus, the FSE is rewritten in the domain $(x', \xi) \in \mathbb{R} \times [0, 1]$ as:

$$\frac{\partial}{\partial x'}(Lu) + \frac{\partial}{\partial \xi}\left(w + u\Xi_x\right) = 0 \tag{3.12a}$$

$$\frac{\partial}{\partial t'}(Lu) + \frac{\partial}{\partial x'}\left(Lu^2 + \frac{1}{2}gL^2 + Lq\right) + \frac{\partial}{\partial \xi}\left(\vartheta u + \Xi_x q\right) = gL\frac{\partial}{\partial x}(L - \eta) \tag{3.12b}$$

$$\frac{\partial}{\partial t'}(Lw) + \frac{\partial}{\partial x'}\left(Luw\right) + \frac{\partial}{\partial \xi}\left(\vartheta w + q\right) = 0 \tag{3.12c}$$

$$\text{BC: } \widetilde{\vartheta} = \widehat{\vartheta} = \widetilde{q} = 0 \tag{3.12d}$$

We dub the above system the Generalized-Coordinate Euler system (GCE).

From this point forward, in order to shorten the notation, the primes when the coordinates x', t' are referenced are dropped.

3.2.1 Getting the SCE from the GCE

A quick inspection reveals that the SCE in the form of eq.(2.17) and the GCE in the form of eq.(3.12) are extremely similar. Indeed, if ones sets $\mathcal{P}_\Xi = -h + \xi H$ (i.e.

$L = H, \forall \xi \in [0,1]$), the two coordinate transformations coincide and the two systems are fully equivalent.

Note that the equality $L = H$ also implies $L_j = H, \forall j$. This is indeed compatible with the nature of the L_j because, by the definition of eq.(3.3), the water column height is written as a convex combination of the layer indicators:

$$H = \sum_{j=0}^{N_l-1} l_j L_j \qquad \text{with:} \quad \sum_{j=0}^{N_l-1} l_j = 1 \tag{3.13}$$

Another insightful equality is:

$$\frac{\sigma_{j+1}(x,t) - \sigma_j(x,t)}{l_j} = \frac{L_j(x,t)}{H(x,t)} \tag{3.14}$$

$$\text{where: } \sigma_j = (z_j + h)/H \tag{3.15}$$

Based on that, if the layer indicators are close to each other (i.e. $L_j \approx H$), then the l_j represent the spacing of the layers in the σ coordinate system: $l_j \approx \sigma_{j+1} - \sigma_j$.

That being said, the layer-wise approach produces systems that are generalizations of the regular σ transformation by adding additional degrees of freedom through the inner layer interfaces $\{z_j(x,t)\}_{j=1}^{N_l-2}$.

An even more general framework is presented in Appendix A, where both transformations are produced as special cases of a broader approach.

3.2.2 Variable reconfiguration

Although the set in the form of eq.(3.12) appears to be in a convenient form, the variable ϑ must be defined explicitly. If this is achieved through eq.(3.11), both velocities u, w are involved, thus further complicating the system.

In order to eliminate the vertical velocity w from the definition of ϑ, we use the continuity equation, alongside the the bottom boundary condition:

$$\left\{ \begin{matrix} \vartheta = w + u\Xi_x + \Xi_t \\ \widehat{\vartheta} = 0 \end{matrix} \right\} \overset{(3.12a)}{\iff} \left\{ \begin{matrix} \vartheta = -\int_0^\xi \left[\frac{\partial L}{\partial t} + \frac{\partial}{\partial x}(Lu) \right] d\xi \\ \widehat{w} + \widehat{u}\widehat{\Xi_x} = 0 \end{matrix} \right\} \iff \tag{3.16}$$

$$\iff \left\{ \begin{matrix} \frac{\partial L}{\partial t} + \frac{\partial}{\partial x}(Lu) + \frac{\partial \vartheta}{\partial \xi} = 0 \\ \widehat{\vartheta} = 0 \\ \widehat{w} + \widehat{u}\widehat{\Xi_x} = 0 \end{matrix} \right\} \tag{3.17}$$

Incorporating eq.(3.17) into the set of eq.(3.12) allows the GCE to be rewritten in the following form:

$$\frac{\partial U}{\partial t} + \frac{\partial}{\partial x}F(U) + \frac{\partial}{\partial \xi}G(U,\vartheta) + \nabla_{x\xi}[q;L] = S(U) \tag{3.18a}$$

$$div(U) = 0 \tag{3.18b}$$

$$\text{BC: } \widetilde{\vartheta} = \widehat{\vartheta} = \widetilde{q} = 0 \tag{3.18c}$$

$$\widehat{w} + \widehat{u}\widehat{\Xi_x} = 0 \tag{3.18d}$$

The primary variables are noted as $U = \begin{bmatrix} L & P & Q \end{bmatrix}^T = \begin{bmatrix} L & Lu & Lw \end{bmatrix}^T$ and the rest of the terms are given by:

$$F(U) = \begin{bmatrix} Lu \\ Lu^2 + \frac{1}{2}gL^2 \\ Luw \end{bmatrix} \tag{3.19a}$$

$$S(U) = \begin{bmatrix} 0 \\ gL\dfrac{\partial}{\partial x}(L-\eta) \\ 0 \end{bmatrix} \tag{3.19b}$$

$$G(U;\vartheta) = \begin{bmatrix} \vartheta \\ \vartheta u \\ \vartheta w \end{bmatrix} \tag{3.19c}$$

$$\nabla_{x\xi}[q;L] = \begin{bmatrix} 0 \\ \dfrac{\partial}{\partial x}(Lq) + \dfrac{\partial}{\partial \xi}(\Xi_x q) \\ \dfrac{\partial q}{\partial \xi} \end{bmatrix} \tag{3.19d}$$

$$div(U) = \frac{\partial}{\partial x}(Lu) + \frac{\partial}{\partial \xi}(w + u\Xi_x) \tag{3.19e}$$

Note that the GCE in the form of eq.(3.18),(3.19) is free of any additional definitions aside from that of Ξ_x given in eq.(3.7c) as the slope of the iso-ξ surfaces.

3.3 Layer kinematics

Having formulate the GCE, we now need to produce a layer kinematic scheme. In order to reveal the underlying physics and the role of $\vartheta_j = \vartheta_{\xi=\xi_j}$, eq.(3.17) is integrated in an arbitrary layer $[\xi_j, \xi_{j+1}]$:

$$\frac{\partial L_j}{\partial t} + \frac{\partial}{\partial x}(Lu)_j + \frac{\vartheta_{j+1} - \vartheta_j}{l_j} = 0 \tag{3.20}$$

$$\text{where: } (Lu)_j \overset{\text{def}}{=\!=} \frac{1}{l_j}\int_{\xi_j}^{\xi_{j+1}} (Lu)d\xi \tag{3.21}$$

As mentioned, eq.(3.20) reveals the main role of the parameter ϑ_j, as it represents the amount of mass that gets transferred between layers $j-1$ and j. Setting $\vartheta_j = 0$ means that the horizontal flux of mass results in the evolution of the layer's height as in:

$$\frac{\partial L_j}{\partial t} + \frac{\partial}{\partial x}(Lu)_j = 0 \tag{3.22}$$

The main advantage of this approach is that by simply moving the layers in the aforementioned way, the ξ-advection becomes unnecessary and the free surface kinematic condition is satisfied implicitly. This approach is essentially a Lagrangian one, as the layer indicators are fully incorporated into the system and are freely evolved in time and space.

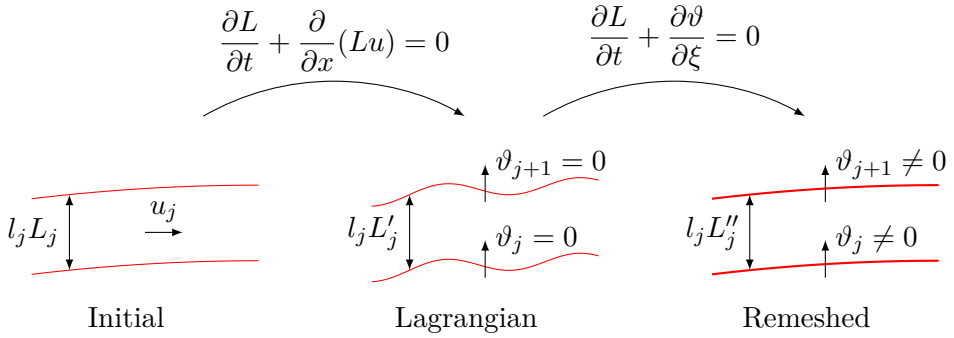

Figure 3.2: The layer kinematic scheme

On top of that, one may follow the Lagrangian evolution by a remeshing step. Within that, the layers are forced into a prescribed shape, thus resulting in mass exchange between the layers. This is expressed by the second part of eq.(3.20):

$$\frac{\partial L_j}{\partial t} + \frac{\vartheta_{j+1} - \vartheta_j}{l_j} = 0 \tag{3.23}$$

It must be noted that this Lagrangian technique followed by an (optional) remeshing falls within the VLR framework mentioned in §3.1 and reviewed in [37].

In order to present a kinematically compatible scheme, the Lagrangian and remeshing steps are incorporated into the x and ξ advection steps respectively.

3.4 The operator splitting formulation

An approach to handle multidimensional problems with pressure coupling is the well-known projection method of Chorin [22, 41], where the advection terms are splitted from the pressure ones. The multidimensional advection is handled through the dimensional splitting technique (see e.g. [42, §19.5]).

This standard operator splitting technique, combined with the layer kinematic scheme (see Figure 3.2) as it was discussed in the previous section, splits the system of eq.(3.18) into the three main operators and the **Semi-Lagrangian Splitting scheme (SLS)** is formed:

1. The x advection, alongside the Lagrangian layer updating:

$$\frac{\partial U}{\partial t} + \frac{\partial}{\partial x} F(U) = S(U) \tag{3.24a}$$

2. The ξ advection, alongside the vertical remeshing:

$$\frac{\partial U}{\partial t} + \frac{\partial}{\partial \xi} G(U, \vartheta) = 0 \tag{3.25a}$$

$$\text{BC: } \widetilde{\vartheta} = \widehat{\vartheta} = 0 \tag{3.25b}$$

3. The pressure correction step, in which the layers are considered static:

$$\frac{\partial U}{\partial t} + \nabla_{x\xi}[q; L] = 0 \tag{3.26a}$$

$$div(U) = 0 \tag{3.26b}$$

$$\text{BC: } \widetilde{q} = 0 \tag{3.26c}$$

$$\widehat{w} + \widehat{u}\widehat{\Xi_x} = 0 \tag{3.26d}$$

3.5 Discretization of variables

In order to present the discrete scheme, we consider the orthogonal tessellation of the domai $\Omega = [a, b] \times [0, 1] \subset \mathbb{R}^2$ that consists of $N = N_x \times N_l$ cells:

$$\Omega = \bigcup_{(i,j)\in\mathcal{I}} \Omega_{ij} \qquad \text{with:} \quad \mathcal{I} = \left\{(i, j) \in \mathbb{N}^2 : 0 \leq i < N_x \text{ and } 0 \leq j < N_l\right\} \tag{3.27}$$

$$\text{where: } \Omega_{ij} = [x_i, x_{i+1}] \times [\xi_j, \xi_{j+1}] \tag{3.28}$$

The cell edges are spaced (see Figure 3.3) in the following way:

$$\Delta x_i = x_{i+1} - x_i \tag{3.29}$$

$$l_j = \xi_{j+1} - \xi_j \tag{3.30}$$

Note that the ξ partition is consistent with the definition of ξ_j, l_j in §3.2.

In order to produce the discrete cell-averaged variables U_{ij} we integrate:

$$U_{ij}(t) = \frac{1}{\Delta x_i \times l_j} \int_{\xi_j}^{\xi_{j+1}} \int_{x_i}^{x_{i+1}} U(x, \xi, t) dx d\xi \tag{3.31}$$

While the double index i, j implies integration in both arguments x, ξ, the semi-discrete forms will also be used:

$$U_i(\xi, t) = \frac{1}{\Delta x_i} \int_{x_i}^{x_{i+1}} U(x, \xi, t) dx \tag{3.32}$$

$$U_j(x, t) = \frac{1}{l_j} \int_{\xi_j}^{\xi_{j+1}} U(x, \xi, t) d\xi \tag{3.33}$$

Note that this notation is consistent with eq.(3.8).

Thus, the primary variables $U_{ij} = [L_{ij}, P_{ij}, Q_{ij}] = [L_{ij}, (Lu)_{ij}, (Lw)_{ij}]^T$ are defined in a cell-averaged way. On the other hand, the variables q, ϑ are placed on the faces of the cells:

$$\vartheta_j(x, t) = \vartheta(x, \xi_j, t) \tag{3.34}$$

$$\vartheta_{ij}(t) = \frac{1}{\Delta x_i} \int_{x_i}^{x_{i+1}} \vartheta_j(x, t) dx \tag{3.35}$$

and:

$$q_i(\xi, t) = q(x_i, \xi, t) \tag{3.36}$$

$$q_{ij}(t) = \frac{1}{l_j} \int_{\xi_j}^{\xi_{j+1}} q_i(\xi, t) d\xi \tag{3.37}$$

The velocity ϑ is placed in the layer interfaces in accordance with eq.(3.20) and the pressure q is placed in the vertical faces for reasons that will be presented in §6.2.

Regarding the temporal resolution, timestepping over the discrete intervals $[t^n, t^{n+1}]$ with $\Delta t^n \stackrel{\text{def}}{=\!=} t^{n+1} - t^n$ is used. The variables at each timestep are noted as:

$$U^n(x, \xi) = U(x, \xi, t^n) \tag{3.38}$$

The same notation $(\cdot)^n$ is used for the discrete and the semi-discrete forms.

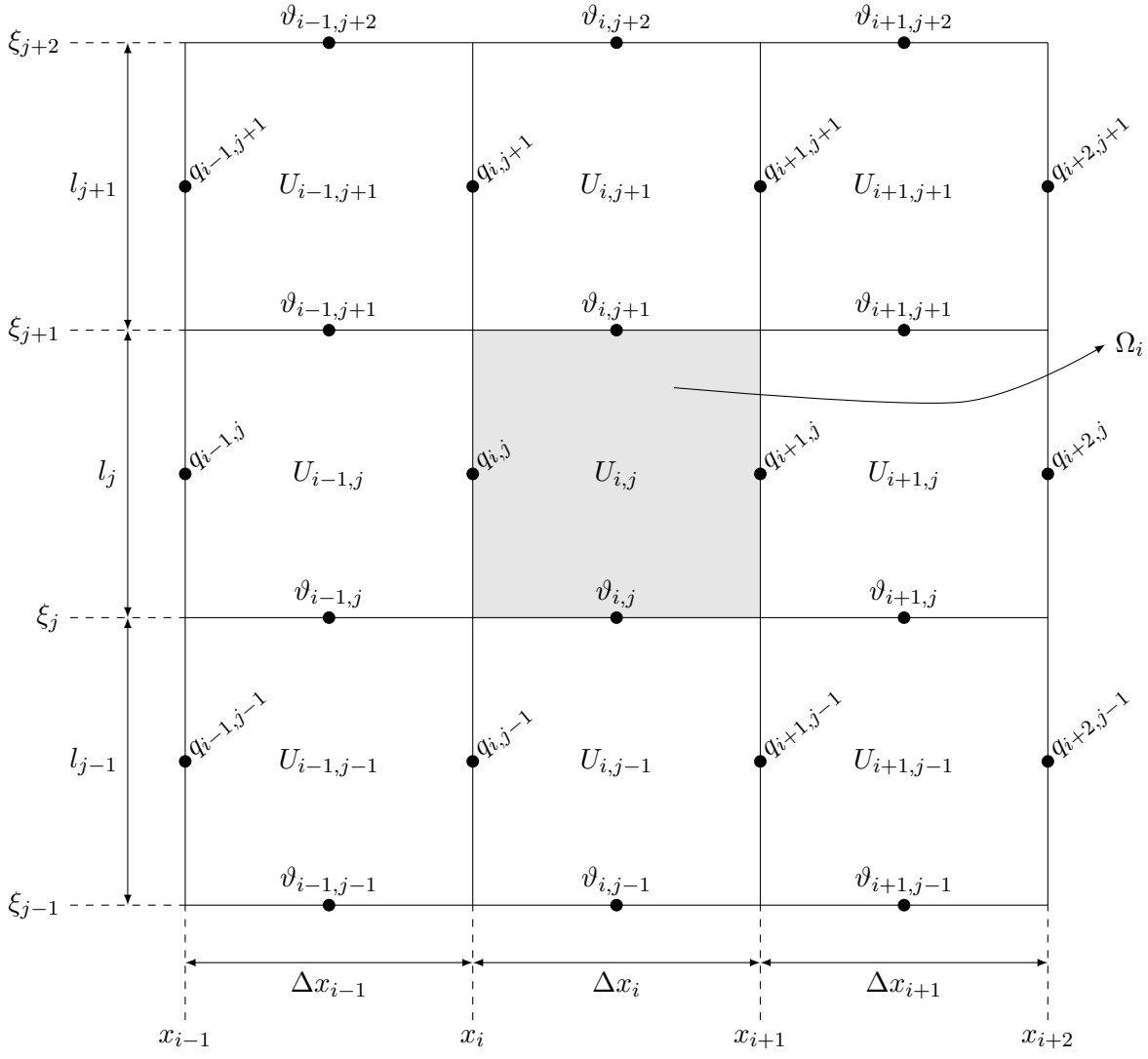

Figure 3.3: Variable indexing on the 2D mesh

3.6 The discrete Semi-Lagrangian Splitting scheme

Having discussed the discretization of variables in the computational mesh, the discrete forms of the three main operators are presented. The operators associated with the x and ξ advection are averaged with respect to only one variable, while the pressure correction step is presented in its continuous form.

(1/3): The operator of eq.(3.24) in the j-discrete form is:

$$\frac{\partial}{\partial t}(L_j) + \frac{\partial}{\partial x}(L_j u_j) = 0 \tag{3.39a}$$

$$\frac{\partial}{\partial t}(L_j u_j) + \frac{\partial}{\partial x}\left(L_j u_j^2 + \frac{1}{2} g L_j^2\right) = g L_j \frac{\partial}{\partial x}(L_j - \eta) \tag{3.39b}$$

$$\frac{\partial}{\partial t}(L_j w_j) + \frac{\partial}{\partial x}\left(L_j u_j w_j\right) = 0 \tag{3.39c}$$

This is nothing but the Multilayer Shallow Water Equations (mSWE) found in [43, 44] and other sources. Chapter 4 is dedicated to its numerical solution.

(2/3): The operator of eq.(3.25) in the i-discrete form is:

$$\frac{\partial}{\partial t}(L_i) + \frac{\partial}{\partial \xi}(\vartheta_i) = 0 \tag{3.40a}$$

$$\frac{\partial}{\partial t}(L_i u_i) + \frac{\partial}{\partial \xi}(\vartheta_i u_i) = 0 \tag{3.40b}$$

$$\frac{\partial}{\partial t}(L_i w_i) + \frac{\partial}{\partial \xi}(\vartheta_i w_i) = 0 \tag{3.40c}$$

$$\text{BC: } \widehat{\vartheta}_i = \widetilde{\vartheta}_i = 0 \tag{3.40d}$$

We dub this the Vertical Remeshing Operator (VRO). It is recognised to be a hyperbolic conservation law and its numerical treatment will be described in detail in Chapter 5.

(3/3): The pressure correction step of eq.(3.26) in the fully continuous form is:

$$\frac{\partial}{\partial t}(Lu) + \frac{\partial}{\partial x}(Lq) + \frac{\partial}{\partial \xi}\left(\Xi_x q\right) = 0 \tag{3.41a}$$

$$\frac{\partial}{\partial t}(Lw) + \frac{\partial q}{\partial \xi} = 0 \tag{3.41b}$$

$$\frac{\partial}{\partial x}(Lu) + \frac{\partial}{\partial \xi}\left(w + u\Xi_x\right) = 0 \tag{3.41c}$$

$$\text{BC: } q_{\xi=1} = 0 \tag{3.41d}$$

$$\left(w + u\Xi_x\right)_{\xi=0} = 0 \tag{3.41e}$$

This operator is noted as the Pressure Correction Operator (PCO). Its discrete form will be discussed in detail in Chapter 6.

Chapter 4

The Multilayer Shallow Water Equations

The scope of this chapter is to fully describe the numerical method used for the solution of the Multilayer Shallow Water Equations (mSWE), as expressed by eq.(3.39):

$$\frac{\partial}{\partial t}(L_j) + \frac{\partial}{\partial x}(L_j u_j) = 0 \tag{4.1a}$$

$$\frac{\partial}{\partial t}(L_j u_j) + \frac{\partial}{\partial x}\left(L_j u_j^2 + \frac{1}{2} g L_j^2\right) = g L_j \frac{\partial}{\partial x}(L_j - \eta) \tag{4.1b}$$

$$\frac{\partial}{\partial t}(L_j w_j) + \frac{\partial}{\partial x}\left(L_j u_j w_j\right) = 0 \tag{4.1c}$$

$$\text{where: } \eta = H - h = \left(\sum_{j=0}^{j<N_l} l_j L_j\right) - h \tag{4.1d}$$

The main feature of the mSWE (that makes its numerical solution somehow difficult) is the genuine loss of hyperbolicity that occurs through the appearance of complex eigenvalues. This loss of hyperbolicity appears in a lot of relevant flow scenarios and is closely related to the well-known Kelvin-Helmholtz instabilities [45]. The eigenstructure of the two-layer model is presented in Appendix B.

The mSWE in its eq.(4.1) form was introduced by Audusse [43] and since then, many schemes have been proposed for its solution [46, 47]. Although schemes that treat the loss of hyperbolicity do exist for the two-layer case [48, 49], their extension to an arbitrary number of layers can be quite cumbersome.

In the present method, the scheme that will be used for the mSWE is based on the uncoupled solver introduced in [50, 44], where the the mSWE is split into its single-layer

counterparts, that are then solved independently. This greatly simplifies the scheme, but special care must be taken when stability is concerned.

The numerical approach to the standard single-layer Shallow Water Equations (SWE) is described in the following section.

4.1 The Shallow Water Equations solver

Our main focus is on the Shallow Water Equations (SWE) with a passive tracer w and bottom topography $h(x)$.

$$\frac{\partial H}{\partial t} + \frac{\partial}{\partial x}(Hu) = 0 \tag{4.2a}$$

$$\frac{\partial}{\partial t}(Hu) + \frac{\partial}{\partial x}\left(Hu^2 + \frac{1}{2}gH^2\right) = \frac{\partial h}{\partial x}gH \tag{4.2b}$$

$$\frac{\partial}{\partial t}(Hw) + \frac{\partial}{\partial x}(Huw) = 0 \tag{4.2c}$$

or in the short-hand operator notation:

$$\frac{\partial U}{\partial t} + \frac{\partial}{\partial x}F(U) = S(U;h) \tag{4.3a}$$

$$\text{with: } F(U) = [F_H\ ,\ F_P\ ,\ F_Q]^T = \left[P\ ,\ P^2/H + gH^2/2\ ,\ PQ/H\right]^T \tag{4.3b}$$

$$S(U;h) = [S_H\ ,\ S_P\ ,\ S_Q]^T = \left[0\ ,\ \frac{\partial h}{\partial x}gH\ ,\ 0\right]^T \tag{4.3c}$$

where $U = [H, P, Q]^T = [H, Hu, Hw]^T$ are the conserved variables, $F(U)$ the flux vector and $S(U;h)$ the topography induced source term.

Remark: The notation used in the description of the SWE solver (i.e. within §4.1) is of a local nature. Thus, some inconsistencies with the rest of the thesis arise (for example $U(x,\xi,t) = [L, Lu, Lu]^T$ is replaced by $U(x,t) = [H, Hu, Hw]^T$). This change is adopted because it lightens the notation and follows the one usually used in the study of SWE systems. That, though, will not affect the analysis of the broader scheme, because the SWE solver is presented in a vacuum and it is only utilized in the mSWE scheme (see §4.2), where compatibility is restored by carefully defining the input-arguments that are passed from one solver to another.

4.1.1 Eigenstructure of the SWE

Defining the celerity $c = \sqrt{gH}$ the Jacobian matrix of the flux is computed as:

$$J_F = \frac{\partial F}{\partial U} = \begin{bmatrix} 0 & 1 & 0 \\ c^2 - u^2 & 2u & 0 \\ -uw & w & u \end{bmatrix} \tag{4.4}$$

after some straight-forward calculations one attains the diagonal matrix Λ_F containing the eigenvalues λ_i of Jacobian and K_F the matrix consisting of its right eigenvectors $K_F^{(i)}$:

$$\Lambda_F = \begin{bmatrix} \lambda_1 & 0 & 0 \\ 0 & \lambda_2 & 0 \\ 0 & 0 & \lambda_3 \end{bmatrix} = \begin{bmatrix} u & 0 & 0 \\ 0 & u+c & 0 \\ 0 & 0 & u-c \end{bmatrix} \tag{4.5}$$

$$K_F = \begin{bmatrix} K_F^{(1)} & K_F^{(2)} & K_F^{(3)} \end{bmatrix} = \begin{bmatrix} 0 & 1 & 1 \\ 0 & u+c & u-c \\ 1 & w & w \end{bmatrix} \tag{4.6}$$

In order to check the hyperbolicity of the system (see [51, §2.4.3]), we compute the quantities:

$$\left[\frac{\partial \lambda_1}{\partial U}\right]^T K_F^{(1)} = 0 \tag{4.7}$$

$$\left[\frac{\partial \lambda_2}{\partial U}\right]^T K_F^{(2)} = \frac{3g}{2c} \tag{4.8}$$

$$\left[\frac{\partial \lambda_3}{\partial U}\right]^T K_F^{(3)} = -\frac{3g}{2c} \tag{4.9}$$

which verifies that for $H \neq 0$ the fields corresponding to the eigenvalues $\lambda_{2,3} = u \pm c$ are genuinely nonlinear, whereas the one relating to $\lambda_1 = u$ is linearly degenerate, which derives from the fact that w is passively advected without inferring in the underlying dynamics of the system.

Another noteworthy property is that $det\,(K_F) = -2c$ that proves that for $H \neq 0$ the eigenvectors are linearly independent.

4.1.2 The finite volume scheme

Let us consider the tessellation $\bigcup_{i=0}^{N-1}[x_i, x_{i+1}]$ (as it was introduced in §3.5), based on which a standard Finite Volume discretization is performed:

$$\frac{\partial U_i}{\partial t} + \frac{\widetilde{F}_{i+1/2} - \widetilde{F}_{i-1/2}}{\Delta x_i} = S_i \tag{4.10}$$

where $\widetilde{F}_{i+1/2} = \widetilde{F}\left(U^L_{i+1/2}, U^R_{i+1/2}\right)$ a suitably defined intercell flux and S_i an approximation of the source term $S(U;h)$.

The left and right state quantities $U^R_{i+1/2}, U^L_{i+1/2}$ are extracted from their cell-averaged counterparts $U_i = \frac{1}{\Delta x_i}\int_{x_i}^{x_{i+1}} U dx$ through a carefully chosen variable reconstruction.

4.1.3 Roe's Riemann solver

As it is customary in the context of Finite Volume methods, the intercell flux is defined by considering the solution of the associated Riemann problem. For an extensive overview of Riemann solvers and their application on numerical methods we refer to [51].

In the context of the present scheme, the approximate Riemann solver of Roe [52] is utilized because of its versatility and mathematical robustness. Roe's method is derived by exactly solving a linearized version of the Riemann problem:

$$\frac{\partial U}{\partial t} + \frac{\partial F}{\partial x} = 0 \xrightarrow{\text{linearize}} \frac{\partial U}{\partial t} + A_{Roe}\frac{\partial U}{\partial x} = 0 \qquad , \quad U(x,0) = \begin{cases} U_R & x > 0 \\ U_L & x < 0 \end{cases} \tag{4.11}$$

The matrix $A_{Roe}(U_L, U_R)$ is not explicitly defined, but is restricted by the following conditions [51, §11.1.2]:

1. Hyperbolicity of the system: A_{Roe} must have real eigenvalues and linearly independent right eigenvectors.
2. Consistency with the Jacobian of the flux: $A_{Roe}(U,U) = J_F(U)$
3. Conservation of discontinuities: $F(U_R) - F(U_L) = \left[A_{Roe}(U_R, U_L)\right](U_R - U_L)$

Omitting the technical details (see [52] and [51] for a formal derivation), the intercell flux in the context of Roe's method is calculated as:

$$\widetilde{F}(U_L, U_R) = \frac{F(U_L) + F(U_R)}{2} - \left[\widetilde{A}(U_L, U_R)\right]\frac{U_R - U_L}{2} \tag{4.12}$$

$$\text{with: } \widetilde{A} \overset{\text{def}}{=\!=} K_{Roe}|\Lambda_{Roe}|K^{-1}_{Roe} \tag{4.13}$$

where: Λ_{Roe} is the diagonal matrix containing the eigenvalues of the the Roe matrix and K_{Roe} the matrix consisting of it's right eigenvectors: $\Lambda_{Roe}, K_{Roe} = eig(A_{Roe})$.

The above methodology is now applied to the SWE system.

A common choice of the Roe matrix is the Jacobian itself computed in an intermediate state $\widetilde{U}$:

$$A_{Roe} = J_F\left(\widetilde{U}\right) = J_F\left(\widetilde{H}\ ,\ \widetilde{H}\widetilde{u}\ ,\ \widetilde{H}\widetilde{w}\right) \tag{4.14}$$

The intermediate state that is consistent with the above choice of A_{Roe}, following the literature about similar systems (see e.g. [53]), is:

$$\widetilde{H} = \frac{H_L + H_R}{2} \tag{4.15a}$$

$$\widetilde{u} = \frac{u_L\sqrt{H_L} + u_R\sqrt{H_R}}{\sqrt{H_L} + \sqrt{H_R}} \tag{4.15b}$$

$$\widetilde{w} = \frac{w_L\sqrt{H_L} + w_R\sqrt{H_R}}{\sqrt{H_L} + \sqrt{H_R}} \tag{4.15c}$$

This averaging is proved to satisfy the 3 requirements mentioned above.

Thus, after some algebraic manipulations, the Roe viscosity matrix can be computed as:

$$\widetilde{A} \overset{\text{def}}{=\!=} K_{Roe}|\Lambda_{Roe}|K_{Roe}^{-1} = \begin{bmatrix} \widetilde{c}(a - bFr) & b & 0 \\ b\widetilde{c}^2(1 - Fr^2) & \widetilde{c}(a + bFr) & 0 \\ \widetilde{c}\widetilde{w}(a - bFr - |Fr|) & b\widetilde{w} & \widetilde{c}|Fr| \end{bmatrix} \tag{4.16}$$

with the Froude number related quantities defined as

$$\widetilde{c} = \sqrt{g\widetilde{H}} \tag{4.17a}$$

$$Fr = \widetilde{u}/\widetilde{c} \tag{4.17b}$$

$$a = \frac{|Fr + 1| + |Fr - 1|}{2} \tag{4.17c}$$

$$b = \frac{|Fr + 1| - |Fr - 1|}{2} \tag{4.17d}$$

4.1.4 Second order reconstruction and slope limiters

In the present section the linear reconstruction scheme is presented. The approach is kept general and within the broad framework of variable reconstruction used in Total Variance Diminishing (TVD) second order Finite Volume schemes. For an extensive analysis of the subject of high order TVD methods we refer to [51, Ch.14].

Let us consider the set $\mathbf{y} = \{y_i\}_{i=0}^{N-1}$ that represents the cell-averaged values of an arbitrary function $y(x)$ on the tessellation $\bigcup_{i=0}^{N-1}[x_i, x_{i+1}]$.

It is obvious that for a given set of values y_i the original function cannot be uniquely retrieved. Choosing a piecewise linear reconstruction, we observe that any function of the type:

$$y_{rec}(x) = y_i + \Delta_i \left(x - \frac{x_i + x_{i+1}}{2} \right) \qquad , \quad x \in [x_i, x_{i+1}] \tag{4.18}$$

conserves the average values for every choice of the in-cell slopes $\{\Delta_i\}_{i=0}^{N-1} \in \mathbb{R}$.

As a first step, one may define the (unlimited) slopes in the central-upwind manner:

$$\Delta_i^* = \frac{1}{2}(1+\omega)\Delta_{i-1/2} + \frac{1}{2}(1-\omega)\Delta_{i+1/2} \tag{4.19}$$

where $\Delta_{i+1/2} = \dfrac{y_{i+1} - y_i}{(\Delta x_{i+1} + \Delta x_i)/2}$ and $\omega \in [-1, 1]$ being a free parameter.

Even if those slopes appear to be the obvious choice, their use in Finite Volume schemes induces spurious oscillations around large gradients/discontinuities and leads to unstable numerical schemes. In order to avoid that, a stable TVD scheme can be constructed if those values are modified through the use of *slope limiters*. The limited slopes are then defined as:

$$\begin{aligned} \Delta_i &= \Delta_i^* \times \min \left\{ \; lim\left(\frac{\Delta_{i-1/2}}{\Delta_i^*} \right) \; , \; lim\left(\frac{\Delta_{i+1/2}}{\Delta_i^*} \right) \; \right\} = \\ &= sign(\Delta_i^*) \times \min \left\{ \; \phi\left(\Delta_{i-1/2} \; , \Delta_i^*\right) \; , \; \phi\left(\Delta_{i+1/2}, \Delta_i^*\right) \; \right\} \end{aligned} \tag{4.20}$$

where $lim : \mathbb{R} \mapsto \mathbb{R}$ an unspecified slope limiter function and $\phi(a,b) \overset{\text{def}}{=\!=} lim\left(\dfrac{a}{b}\right)|b|$.

Exploiting the property that $lim(r) = 0, \; \forall r \leq 0$ the function ϕ is rewritten:

$$\phi(a,b) = \begin{cases} lim\left(\dfrac{|a|}{|b|}\right)|b| & ab \geq 0 \\ 0 & ab < 0 \end{cases}$$

In the present work the Van Albada [54] limiter is used:

$$lim_{Albada}(r) = \begin{cases} \dfrac{r^2 + r}{r^2 + 1} & r \geq 0 \\ 0 & r < 0 \end{cases} \tag{4.21}$$

which produces:

$$\phi_{Albada}(a, b; \epsilon) = \begin{cases} \dfrac{(a^2 + \epsilon)|b| + (b^2 + \epsilon)|a|}{(a^2 + \epsilon) + (b^2 + \epsilon)} & ab \geq 0 \\ 0 & ab < 0 \end{cases} \tag{4.22}$$

where ϵ following [55] and [54] is a small number to avoid division by zero in the (relevant) case of vanishing slopes and also to enhance the convergence properties. Such enhancement can be achieved [56] by setting $\epsilon = K^3 \Delta x$ where $K \approx 5$.

Summarizing the procedure presented, the slopes are defined solely based on the cell averages (i.e. $y_i \mapsto \Delta_i^* \mapsto \Delta_i$). Thus, the inter-cell values of the reconstructed function can be computed as:

$$y_{i+1/2}^R = \lim_{x \to x_{i+1}^+} y_{rec}(x) = y_{i+1} - \Delta_{i+1} \frac{\Delta x_{i+1}}{2} \tag{4.23}$$

$$y_{i+1/2}^L = \lim_{x \to x_{i+1}^-} y_{rec}(x) = y_i + \Delta_i \frac{\Delta x_i}{2} \tag{4.24}$$

The reconstruction operator that returns those values can then be written as:

$$\mathbf{y}^{L/R} = \mathcal{R}_{lim}^2(\mathbf{y}) \tag{4.25}$$

The superscript L/R is used to merge the left and right intercell values in order to shorten the notation.

One important property is that this reconstruction operator leaves a set of constant values unaffected:

$$\{y_i = y_j \ , \ \forall i, j\} \Longrightarrow \mathbf{y} = \mathcal{R}_{lim}^2(\mathbf{y}) \tag{4.26}$$

4.1.5 Hydrostatic reconstruction and source term

An important property of the numerical scheme is its ability to exactly preserve steady states in the discrete level. As this is of tremendous practical importance, the construction of so-called *well-balanced* schemes has been the focus of many researchers. For a more general approach to the construction of such schemes we refer to [57, 58] and the references therein.

In the present method, we focus only on the preservation of the lake-at-rest steady state, where the fluid is motionless ($u = w = 0$) and the free surface horizontal ($H - h = const$). Schemes that preserve this are said to satisfy the C-property (introduced in [59]).

Let us now introduce a set of cell-centered topography values $\mathbf{h} = \{h_i\}_{i=0}^{N-1}$ and a set of nodal values that are defined based on those $\widetilde{\mathbf{h}} = \{\widetilde{h}_{i+1/2}\}_{i=0}^{N-2}$. Having said that, the discrete C-property is expressed:

$$\text{if} \quad \left\{ \begin{matrix} H_i - h_i = C \\ u_i = w_i = 0 \end{matrix} \right\} \quad \text{then:} \quad \left. \frac{\Delta \widetilde{F}}{\Delta x} \right|_i = S_i \Leftrightarrow \frac{\partial U_i}{\partial t} = 0 \tag{4.27}$$

It is readily observed that the C-property relies on balancing the discrete flux and source term of the horizontal momentum equation.

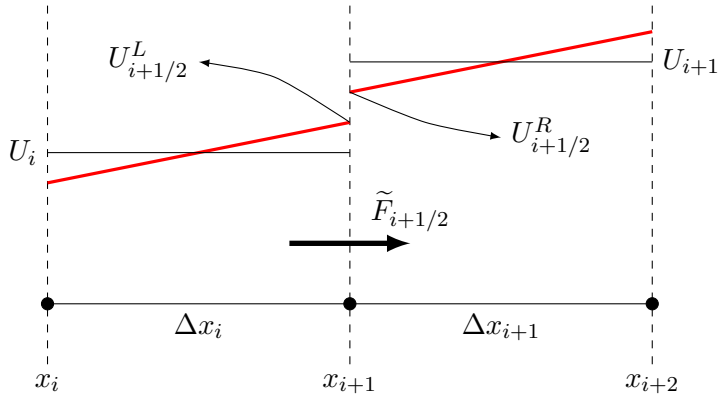

Figure 4.1: SWE variable reconstruction

Bearing that in mind, we now focus on the variable reconstruction process that will be used in the SWE scheme. As it is presented in Figure 4.1 the interface values $(\cdot)^{L/R}_{i+1/2}$ must be extracted from their cell-centered counterparts $(\cdot)_i$ in order to be used in the numerical flux $\widetilde{F}_{i+1/2}$.

Following [60] and using the second order operator $\mathcal{R}^2_{lim}$ presented in §4.1.4, the fol-

lowing reconstruction is proposed:

$$\mathbf{H}^{L/R} = \mathcal{R}^2_{lim}\left(\mathbf{H} - \mathbf{h}\right) + \widetilde{\mathbf{h}} \tag{4.28a}$$

$$\mathbf{P}^{L/R} = \mathcal{R}^2_{lim}\left(\mathbf{P}\right) \tag{4.28b}$$

$$\mathbf{Q}^{L/R} = \mathcal{R}^2_{lim}\left(\mathbf{Q}\right) \tag{4.28c}$$

$$\text{or: } \mathbf{U}^{L/R} = \mathcal{R}^{hydro}_{SWE}(\mathbf{U}); \tag{4.28d}$$

Based on that and due to eq.(4.26), in the lake-at-rest state the interface variables are:

$$\left\{ \begin{matrix} H_i - h_i = C \\ P_i = Q_i = 0 \end{matrix} \ , \ \forall i \right\} \Longrightarrow U^L_{i+1/2} = U^R_{i+1/2} = \left[C + \widetilde{h}_{i+1/2} \ , \ 0 \ , \ 0 \right]^T \tag{4.29}$$

Focusing on the x-momentum component and since the intercell flux satisfies the consistency property $\widetilde{F}(U,U) = F(U)$ we compute the horizontal momentum part F_P of the flux:

$$\begin{aligned} &\widetilde{F}^P_{i+1/2} = \frac{1}{2} g (C + \widetilde{h}_{i+1/2})^2 = \frac{1}{2} g C^2 + g C \widetilde{h}_{i+1/2} + \frac{1}{2} g \widetilde{h}^2_{i+1/2} \\ \Rightarrow &\frac{\widetilde{F}^P_{i+1/2} - \widetilde{F}^P_{i-1/2}}{\Delta x_i} = g C \frac{\widetilde{h}_{i+1/2} - \widetilde{h}_{i-1/2}}{\Delta x_i} + \frac{1}{2} g \frac{\widetilde{h}^2_{i+1/2} - \widetilde{h}^2_{i-1/2}}{\Delta x_i} \\ \Rightarrow &\frac{\Delta \widetilde{F}_P}{\Delta x} = g C \frac{\Delta \widetilde{h}}{\Delta x} + \frac{1}{2} g \frac{\Delta (\widetilde{h}^2)}{\Delta x} \end{aligned} \tag{4.30}$$

Now, the momentum source term S_P is rewritten in a similar-looking manner:

$$S_P = gH\frac{\partial h}{\partial x} = g(H-h)\frac{\partial h}{\partial x} + gh\frac{\partial h}{\partial x} = g(H-h)\frac{\partial h}{\partial x} + \frac{1}{2} g \frac{\partial (h^2)}{\partial x} \tag{4.31}$$

Aiming to balance the flux when $H_i - h_i = C$, the discrete source is chosen to be:

$$\frac{1}{\Delta x_i} \int_{x_i}^{x_{i+1}} S_P dx \approx S^P_i = g(H_i - h_i)\frac{\Delta \widetilde{h}}{\Delta x} + \frac{1}{2} g \frac{\Delta (\widetilde{h}^2)}{\Delta x} \tag{4.32}$$

Having defined the variable reconstruction and the source term, eq.(4.30) in conjunction with eq.(4.32) shows that the scheme satisfies the C-property. Note that only the horizontal momentum components were balanced, because the other components are trivially zero in the lake-at-rest state.

The relation between the nodal $\widetilde{h}_{i+1/2}$ and the cell-centered topography values h_i is yet to be specified. Although a lot of valid choices exist, again following [60], an "upwind" approach of the following type is adopted:

$$\widetilde{h}_{i+1/2} = \min\left\{h_i, h_{i+1}\right\} \tag{4.33}$$

The proposed second order hydrostatic reconstruction scheme is presented in detail in Algorithm 1.

4.1.6 Boundary conditions and timestepping

Something yet to be specified is the implementation of the boundary conditions into the SWE solver. For an extensive overview of their incorporation into the Finite Volume framework we refer to [42, Ch.7]. In the present case the use of Dirichlet-type conditions is adopted:

$$U(x_0,t) = U^L_{BC}(t) \qquad \text{and} \qquad U(x_N,t) = U^R_{BC}(t) \tag{4.34}$$

In order to enforce them the standard use of "ghost" nodes is applied: Two fictitious cells are placed on the left and right ends of the computational domain, which are forced to contain the fixed values U^L_{BC}, U^R_{BC} respectively. Those cells are concatenated alongside the regular ones and are used in the variable reconstruction process in order to compute the nodal values $U^L_{i+1/2}, U^R_{i+1/2}$ that used to calculate the intercell fluxes $\widetilde{F}_{i+1/2} = \widetilde{F}\left(U^L_{i+1/2}, U^R_{i+1/2}\right)$.

Let us now consider a timestep $[t^n, t^{n+1}]$ with $\Delta t^n \overset{\text{def}}{=\!=} t^{n+1} - t^n$. The last thing left to be specified is the temporal resolution of the space-discrete conservation law of eq.(4.10). For the sake of simplicity, the first order explicit method is adopted:

$$\mathbf{U}^{n+1} = \mathbf{U}^n + \Delta t^n \mathbf{R}_{SWE}(\mathbf{U}^n, t^n) \tag{4.35}$$

$$\text{where: } (R_i)_{SWE} \overset{\text{def}}{=\!=} S_i - \frac{\widetilde{F}_{i+1/2} - \widetilde{F}_{i-1/2}}{\Delta x_i} \tag{4.36}$$

One major thing to address when using an explicit method is the matter of stability. In a standard fashion, for nonlinear systems (see e.g. [42, Chapter 15]), the standard *CFL condition* is enforced:

$$\Delta t \max_{0\le i<N} \left\{ \frac{(S_{max})_i}{\Delta x_i} \right\} < 1 \tag{4.37}$$

with $S_{max} = \max\{|\lambda_1|, |\lambda_2|, |\lambda_3|\} \overset{(4.5)}{=\!=} |u| + c$ representing the largest eigenvalue.

That means that setting the timestep as

$$\Delta t \leftarrow \mathbb{CFL} \min_{0\le i<N} \left\{ \frac{\Delta x_i}{|P_i/H_i| + \sqrt{gH_i}} \right\} \tag{4.38}$$

ensures the CFL stability of the method when $0 < \mathbb{CFL} < 1$ is chosen.

That being said, the timestepping procedure takes the form:

1. Given a $\mathbb{CFL}$ constant, eq.(4.38) is used to determine the timestep size Δt^n based on the data of the previous step $\mathbf{U}^n$ (at time $t = t^n$). Time progresses accordingly: $t^{n+1} \leftarrow t^n + \Delta t^n$

2. The residual $\mathbf{R}(\mathbf{U}^n, t^n)$ is calculated through the procedure described in Algorithm 2: The boundary conditions are incorporated into the variable reconstruction procedure. The reconstruction is then succeeded by the application of the Roe scheme, as described in the corresponding sections of the present chapter. The source term is calculated by eq.(4.32) so that the discrete C-property is satisfied.

3. The solution is updated $\mathbf{U}^{n+1} \leftarrow \mathbf{U}^n + \Delta t^n \mathbf{R}(\mathbf{U}^n, t^n)$ and the timestepping is repeated.

Algorithm 1 SWE variable reconstruction

Input: $H, P, Q, h, H_{BC}, P_{BC}, Q_{BC}, h_{BC}$

Boundary conditions incorpotated as ghost nodes:
$H = \begin{bmatrix} H^L_{BC} & H_0 & H^R_{BC} \end{bmatrix}$
$P = \begin{bmatrix} P^L_{BC} & P_0 & P^R_{BC} \end{bmatrix}$
$Q = \begin{bmatrix} Q^L_{BC} & Q_0 & Q^R_{BC} \end{bmatrix}$
$h = \begin{bmatrix} h^L_{BC} & h_0 & h^R_{BC} \end{bmatrix}$

Unlimited slope calculation using eq.(4.19):
$\Delta^*_\eta = slope(H - h)$
$\Delta^*_P = slope(P)$
$\Delta^*_Q = slope(Q)$

Slope limiting using eq.(4.20) and eq.(4.22):
$\Delta_\eta = limiter(\Delta^*_\eta, H - h)$
$\Delta_P = limiter(\Delta^*_P, P)$
$\Delta_Q = limiter(\Delta^*_Q, Q)$

for $i = 0, N_x$ **do**
Reconstruction of the nodal topography values using eq.(4.33):
$\widetilde{h}_{i+1/2} = \min\{h_i, h_{i+1}\}$

Calculation of the Left and Right states:
$H^L_{i+1/2} = H_i - h_i + h_{i+1/2} + \Delta_{i,\eta}/2$
$H^R_{i+1/2} = H_{i+1} - h_{i+1} + h_{i+1/2} - \Delta_{i+1,\eta}/2$
$P^L_{i+1/2} = P_i + \Delta_{i,P}/2$
$P^R_{i+1/2} = P_{i+1} - \Delta_{i+1,P}/2$
$Q^L_{i+1/2} = Q_i + \Delta_{i,Q}/2$
$Q^R_{i+1/2} = Q_{i+1} - \Delta_{i+1,Q}/2$
end for
return $\widetilde{h}_{(\cdot)+1/2}, U_R, U_L$

Algorithm 2 SWE residual calculation

Input: $H, P, Q, h, H_{BC}, P_{BC}, Q_{BC}, h_{BC}, g$

Perform the reconstruction algorithm:
$\widetilde{h}_{(\cdot)+1/2}, U_R, U_L \leftarrow SWE\_reconstruction(H, P, Q, h, H_{BC}, P_{BC}, Q_{BC}, h_{BC})$

for $i = 0, N$ **do**
Calculate the Roe average variables using eq.(4.15):
$\widetilde{U} \leftarrow Roe\_average(U_L, U_R)$
Compute the viscosity matrix according to eq.(4.16):
$\widetilde{A} \leftarrow Roe\_viscosity(\widetilde{U})$

Compute the intercell flux
$\widetilde{F}_{i+1/2} \leftarrow \dfrac{F(U_L) + F(U_R)}{2} - \left[\widetilde{A}\right] \dfrac{U_R - U_L}{2}$
end for

for $i = 0, N-1$ **do**
Calculate the source term using eq.(4.32):
$S_P \leftarrow g(H_i - h_i)\dfrac{\widetilde{h}_{i+1/2} - \widetilde{h}_{i-1/2}}{\Delta x_i} + \dfrac{g}{2}\dfrac{\widetilde{h}^2_{i+1/2} - \widetilde{h}^2_{i-1/2}}{\Delta x_i}$
$S_i \leftarrow [0\ ,\ S_P\ ,\ 0]^T$

Extract the residual:
$R_i \leftarrow S_i - \dfrac{\widetilde{F}_{i+1/2} - \widetilde{F}_{i-1/2}}{\Delta x_i}$
end for
return R

4.2 The uncoupled mSWE scheme

The key to the numerical method implemented here is to write the mSWE as:

$$\frac{\partial U_j}{\partial t} + \frac{\partial}{\partial x} F(U_j) = S(U_j; L_j - \eta) \tag{4.39}$$

where: $U_j = \begin{bmatrix} L_j & L_j u_j & L_j w_j \end{bmatrix}^T$ and $F(U), S(U;h)$ are the flux and source term of the regular SWE as described in eq.(4.3).

This loss of hyperbolicity is due to the fact that the topography gradient in the source term is dependant on layer indicators L_j :

$$S_j = S(U_j; h_j^\circ) = g L_j \frac{\partial h_j^\circ}{\partial x} \tag{4.40}$$

$$\text{where: } h_j^\circ \overset{\text{def}}{=\!=} h + L_j - H = h + L_j - \sum_{j=0}^{j<N_l} l_j L_j \tag{4.41}$$

It can be easily seen that the system becomes a system of uncoupled hyperbolic conservation laws if one forces $L_j = H \ , \ \forall (x,t)$. In order to minimize the cross-layer coupling (i.e. $h_j^\circ \approx h$), the layers are remeshed in a way that results in a low variance of the layer indicators (i.e. $L_j \approx H$) at the start of each timestep. This means that the coupling between the layers is mainly achieved through the VRO and the mSWE are further stabilized. The remeshing strategy will be described in depth in the next chapter.

The restriction that the layer indicators L_j must remain close to the depth H is the main reason that they were defined as $L_j \overset{\text{def}}{=\!=} \Delta z_j / l_j$ (see the discussion of §3.2.1). If the indicators were defined in any other way, utilizing them as a primary variable in the mSWE would result in a dominant cross-layer coupling regardless of the adopted remeshing technique.

Having addressed the cross-layer coupling, one can construct an numerical scheme for the mSWE by the consecutive (and uncoupled) solution of N_l regular SWE [50]. As seen in eq.(4.39), the only non-local element is the topography-like term h_j°, that introduces the coupling. In the present timestepping method, this term is calculated by the data provided by the previous timestep and is either updated as the SWE operators are applied or is kept unchanged[1]. Even though those approaches perform almost identically, the non-updating option is adopted herein. The general procedure is outlined in Algorithm 3.

[1] In [44] those are referred to as the *splitting* and *sum* schemes

Algorithm 3 Multilayer Shallow Water Equations solver

Input: $U^n, \Delta t^n, h, U_{BC}^{L/R}$
$H_* \leftarrow \sum_{j=0}^{j<N_l} l_j L_j^n$
for $0 \leq j < N_l$ **do**
  $h_j^\circ \leftarrow h + L_j^n - H_*$
  $U_j^{n+1} \leftarrow U_j^n + \Delta t^n \cdot R_{SWE}\left(U_j^n; h_j^\circ; \left\{U_{BC}^{L/R}\right\}_j\right)$
  if inter-layer updating is chosen **then**
    $H_* \leftarrow H_* + l_j(L_j^{n+1} - L_j^n)$
  end if
end for
  return U^{n+1}

Notes:
The primary variables are noted as $U \overset{\text{def}}{=\!=} [L, Lu, Lw]^T$, while U^n, U^{n+1} denote the variables at time t^n, t^{n+1} respectively.

An important property of this scheme is that if the SWE scheme satisfies the discrete C-property of eq.(4.27), then that property is also valid for the mSWE scheme in the following sense:

$$\left\{\begin{matrix} H_i - h_i = C \\ P_{ij} = Q_{ij} = 0 \end{matrix}\right\} \overset{(4.41)}{\Longleftrightarrow} \left\{\begin{matrix} L_{ij} - h_{ij}^\circ = C \\ P_{ij} = Q_{ij} = 0 \end{matrix}\right\} \overset{\text{C-property}}{\Longrightarrow} R_{SWE}\left(\mathbf{U}_j; \mathbf{h}_j^\circ\right) = 0 \tag{4.42}$$

Chapter 5

The Vertical Remeshing Operator

In this chapter the numerical resolution of the Vertical Remeshing Operator (VRO) is described. Since the dependence on the index i is of a purely parametric nature, the corresponding subscript in the set of eq.(3.40) is dropped:

$$\frac{\partial}{\partial t}(L) + \frac{\partial}{\partial \xi}(\vartheta) = 0 \tag{5.1a}$$

$$\frac{\partial}{\partial t}(Lu) + \frac{\partial}{\partial \xi}(\vartheta u) = 0 \tag{5.1b}$$

$$\frac{\partial}{\partial t}(Lw) + \frac{\partial}{\partial \xi}(\vartheta u) = 0 \tag{5.1c}$$

$$\text{BC: } \widehat{\vartheta} = \widetilde{\vartheta} = 0 \tag{5.1d}$$

Timestepping with initial condition $U^0 = [L, Lu, Lw]^0$ on the interval $t \in [t, t + \Delta t]$ is considered. The final/remeshed values are noted as $U^* = [L, Lu, Lw]^*$.

The eq.(5.1a)-(5.1c) of the VRO can be written in the conservative form:

$$\frac{\partial U}{\partial t} + \frac{\partial}{\partial \xi} G(U; \vartheta) = 0 \qquad \xi \in [0, 1] \tag{5.2}$$

with the flux defined as:

$$G(U; \vartheta) = \frac{\vartheta}{L} U \tag{5.3}$$

Thus, the VRO is identified to be a hyperbolic conservation law where the variables are advected with speed $c = \vartheta / L$.

5.1 Remeshing and kinematic considerations

As it was briefly pointed out in §3.3, the main purpose of the VRO is to act as a correction to the Lagrangian layer kinematics. That means that given the initial layer indicators L_j^0 one must define based on them the remeshed quantities L_j^* in order for the velocities ϑ_j to be defined based on eq.(5.1a). After those are defined, eq.(5.1b),(5.1c) are used to remap the velocities $(Lu, Lw)^0 \mapsto (Lu, Lw)^*$ on the newly defined layers.

Aside from the mathematical standpoint of operator-splitting, the VRO has very clear physical interpretation. After the application of the mSWE the layers are evolved in the Lagrangian manner that indirectly implies that there is no mass exchange between the layers. That mass exchange is directly connected to the ϑ_j that are essentially the velocity normal to the interface between the layers. Thus, it is only natural that if one chooses not to remap the layers (i.e. $L_j^0 = L_j^*$) eq.(5.1a) implies that there is indeed no mass exchange between the layers (i.e. $\vartheta_j = 0$).

Having said that, we integrate eq.(5.1a) over $[t, t + \Delta t] \times [\xi_j, \xi_{j+1}]$ to obtain:

$$\vartheta_{j+1}^* = \begin{cases} \vartheta_j^* - \dfrac{l_j}{\Delta t}\left(L_j^* - L_j^0\right) & , \ j \geq 0 \\ 0 & , \ j = -1 \end{cases} \tag{5.4}$$

where $\vartheta_j^* \overset{\text{def}}{=\!=} \frac{1}{\Delta t}\int_t^{t+\Delta t} \vartheta_j dt$ and $\vartheta_j = \vartheta_{\xi=\xi_j}$.

One last thing of note is the incorporation of the boundary conditions related to the vertical advection as pointed out in eq.(5.1d) (i.e. $\vartheta_0 = \vartheta_{N_l} = 0$). As seen in eq.(5.4) the bottom impermeability condition is directly enforced by setting $\vartheta_0^* = 0$. That is not true for the free surface kinematic condition of $\vartheta_{N_l}^* = 0$, where special care must be taken.

A quick inspection of eq.(5.4) gives:

$$\vartheta_{N_l}^* = 0 \Longleftrightarrow \sum_{j=0}^{j<N_l} l_j L_j^0 = \sum_{j=0}^{j<N_l} l_j L_j^* = H \tag{5.5}$$

We define a remeshing strategy that satisfies the above relation as *kinematically consistent*.

Although a lot of remeshing strategies can be valid, the natural choice, which will be adopted in the present method, is to set all the layer indicators to be equal to the water depth H:

$$L_j^* = H = \sum_{j=0}^{j<N_l} l_j L_j^0 \tag{5.6}$$

This approach, which is dubbed as the *Eulerian remapping*, aside from its simplicity makes sure that the indicators do not stray away from their mean value (i.e. the water depth H). That is (as pointed out in §4.2) extremely important because big deviations from that would result in a strong cross-layer coupling in the mSWE, thus resulting in problems in the numerical method.

5.2 Spatial resolution

In order to discretize the VRO in the time domain, we suppose a set of starting variables U^0 and the target layer indicators L^* that define the ϑ^* through eq.(5.4).

Concerning eq.(5.1b),(5.1c) the explicit Finite Volume formulation of the following type on the tessellation $[0,1] = \bigcup_{j=0}^{N_l-1} [\xi_j, \xi_{j+1}]$ is employed:

$$\mathcal{U}_j^* = \mathcal{U}_j^0 - \frac{\Delta t}{l_j}\left[\widetilde{G}_{j+1/2} - \widetilde{G}_{j-1/2}\right] \tag{5.7}$$

with $\mathcal{U} = [Lu, Lw]^T$ and $\widetilde{G}_{i+1/2} = \widetilde{G}\left(\mathcal{U}_j, \mathcal{U}_{j+1}; \vartheta_{j+1}\right)$ a suitably defined numerical flux.

5.2.1 Flux reconstruction

Having said that, one must define the intercell value $\widetilde{G}$ of the flux $G = \dfrac{\vartheta}{L}\mathcal{U}$ so that eq.(5.1b),(5.1c) can be discretized. Since the only (albeit double) eigenvalue of the flux is the speed $c = \vartheta/L$, the natural choice is the one-wave scheme of Rusanov [61]. Bearing in mind the piecewise constant vertical discretization (as described in §3.6) and the notation displayed in Figure 5.1, the intercell flux takes the following form:

$$\begin{aligned}\widetilde{G}_{j+1/2} &= \frac{c^L_{j+1/2}\mathcal{U}_j + c^R_{j+1/2}\mathcal{U}_{j+1}}{2} - \max\left\{|c^L_{j+1/2}|, |c^R_{j+1/2}|\right\}\frac{\mathcal{U}_{j+1} - \mathcal{U}_j}{2} \\ &= \frac{1}{2}\left(\frac{\vartheta_{j+1}}{L_j} + \frac{|\vartheta_{j+1}|}{L_{j+1/2}}\right)\mathcal{U}_j + \frac{1}{2}\left(\frac{\vartheta_{j+1}}{L_{j+1}} - \frac{|\vartheta_{j+1}|}{L_{j+1/2}}\right)\mathcal{U}_{j+1}\end{aligned} \tag{5.8}$$

,where $\mathcal{U} = [Lu, Lw]^T$ and $L_{j+1/2} \overset{\text{def}}{=\!=} \min\{L_j, L_{j+1}\}$

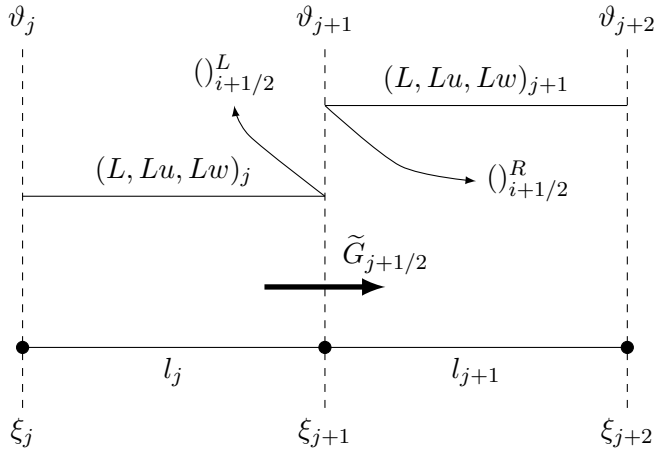

Figure 5.1: VRO variable reconstruction

5.2.2 Boundary conditions

Another important thing to specify is the treatment of boundary conditions and how the interfaces on the outer boundary of the domain are incorporated into the reconstruction process. In the context of Finite Volume methods, usually an assumption must be made concerning the state of variables either on the boundary interface or in the cells just outside the computation domain (as it was discussed in §4.1.6).

In the case of the VRO such an approach is not needed, as it will illustrated. The main advantage of the method is that the nodal values of ϑ_j^* are determined based on the remeshing strategy by using eq.(5.4). That means that those values are defined independently of the calculation of the intercell fluxes $\widetilde{G}$. Furthermore, if a *kinematically consistent* remeshing strategy is employed, the relation $\vartheta_0^* = \vartheta_{N_l}^* = 0$ is automatically satisfied. That, in conjunction with eq.(5.8), gives the very useful relation:

$$\vartheta_0 = \vartheta_{N_l} = 0 \quad \Longrightarrow \quad \widetilde{G}_{-1/2} = \widetilde{G}_{N_l - 1/2} = 0 \tag{5.9}$$

That means that the intercell flux $\widetilde{G}$ on the boundary is zero independently of any assumption made regarding the variables (Lu, Lw) and thus any further treatment becomes unnecessary. Aside from convenience, there is also a physical relevance to that, as no mass exchange (i.e. $\vartheta = 0$) directly implies zero momentum exchange (i.e. $\widetilde{G} = 0$) on the boundary interfaces.

5.3 Temporal resolution and final scheme

Again following the arguments that were laid out in §4.1.6, the *CFL stability* of such an explicit timestepping is ensured when:

$$\Delta t \max_{0 \leq j < N_l} \left\{ \frac{S_j^*}{l_j} \right\} < 1 \tag{5.10}$$

$$\text{with: } S_j^* = \frac{\left| \vartheta_{j+1}^* + \vartheta_j^* \right|}{2L_j^*} \tag{5.11}$$

After that note, the fully discrete VRO can be outlined:

1. The initial condition U^0 is defined alongside the timestep Δt as the input.
2. The target remeshed layer indicators L_j^* are determined by eq.(5.6).
3. The velocities ϑ^* are calculated through eq.(5.4).
4. The intercell fluxes $\widetilde{G}_{j+1/2}$ are calculated through eq.(5.3) in the inner interfaces, while $\widetilde{G} = 0$ is set on the boundaries.
5. The velocities are updated by eq.(5.7): $\mathcal{U}_j^* \leftarrow \mathcal{U}_j^0 - \dfrac{\Delta t}{l_j} \left(\widetilde{G}_{i+1/2} - \widetilde{G}_{i-1/2} \right)$

The process is also described in Algorithm 4.

Algorithm 4 Discrete VRO scheme

Input: $[L, Lu, Lw]^0, \Delta t$

$H^* \leftarrow \sum_{j=0}^{j<N_l} l_j L_j^0$

$\vartheta_0^* \leftarrow 0$
$\widetilde{G}_{-1/2} \leftarrow 0$

$\mathcal{U}^0 \leftarrow [Lu, Lw]^0$

for $0 \leq j < N_l$ **do**
$L_j^* \leftarrow H^*$
$\vartheta_{j+1}^* \leftarrow \vartheta_j^* - \dfrac{l_j}{\Delta t}\left(L_j^* - L_j^0\right)$

if $j = N_l - 1$ **then**
$\widetilde{G}_{i+1/2} = 0$
else
$L_{j+1/2} \leftarrow \min\left\{L_j^*, L_{j+1}^*\right\}$
$a_L \leftarrow \dfrac{1}{2}\left(\dfrac{\vartheta_{j+1}^*}{L_j^*} + \dfrac{|\vartheta_{j+1}^*|}{L_{j+1/2}^*}\right)$
$a_R \leftarrow \dfrac{1}{2}\left(\dfrac{\vartheta_{j+1}^*}{L_{j+1}^*} - \dfrac{|\vartheta_{j+1}^*|}{L_{j+1/2}^*}\right)$
$\widetilde{G}_{j+1/2} \leftarrow a_L \mathcal{U}_i^0 + a_R \mathcal{U}_{i+1}^0$
end if

$\mathcal{U}_j^* \leftarrow \mathcal{U}_j^0 - \dfrac{\Delta t}{l_j}\left(\widetilde{G}_{i+1/2} - \widetilde{G}_{i-1/2}\right)$

end for
return $(L, Lu, Lw, \vartheta)^*$

Chapter 6

The Pressure Correction Operator

In this chapter the numerical scheme for the Pressure Correction Operator (PCO) is described. The PCO, as it was presented in eq.(3.40) is repeated in its fully continuous form.

$$\frac{\partial}{\partial t}(Lu) + \frac{\partial}{\partial x}(Lq) + \frac{\partial}{\partial \xi}(\Xi_x q) = 0 \tag{6.1a}$$

$$\frac{\partial}{\partial t}(Lw) + \frac{\partial q}{\partial \xi} = 0 \tag{6.1b}$$

$$\frac{\partial}{\partial x}(Lu) + \frac{\partial}{\partial \xi}(w + u\Xi_x) = 0 \tag{6.1c}$$

$$q_{\xi=1} = 0 \tag{6.1d}$$

$$(w + u\Xi_x)_{\xi=0} = w_{\xi=0} + u_{\xi=0}\frac{\partial h}{\partial x} = 0 \tag{6.1e}$$

6.1 The partially implicit approach

The general idea behind the projection method of Chorin [22, 41] is to define the pressure field q that if applied to the field $\mathbf{u}^* = [u^*, w^*]^T$ results into a divergence-free velocity field $\mathbf{u} = [u, w]^T$. Again, similar to the previous chapters, the scheme is applied on a finite time window $[t, t + \Delta t]$. The standard procedure for this method is formulated through a simple first order implicit temporal method:

$$\left\{ \begin{array}{c} \dfrac{\mathbf{u} - \mathbf{u}^*}{\Delta t} + \nabla q = 0 \\ \nabla \cdot \mathbf{u} = 0 \end{array} \right\} \Longleftrightarrow \left\{ \begin{array}{c} \mathbf{u} = \mathbf{u}^* - \Delta t\,(\nabla q) \\ \nabla^2 q = \dfrac{\nabla \cdot \mathbf{u}^*}{\Delta t} \end{array} \right\} \tag{6.2}$$

And thus, the pressure field is calculated through the Poisson equation and is then used to update the field.

While this approach is easily implemented in a structured cartesian mesh, its use on the $x-\xi$ system poses some difficulties. The first is related to the extra complexity of the Poisson equation in the transformed coordinate system. The Laplacian operator following eq.(3.9a) in that case is:

$$L^2\left(\nabla^2 q\right) = L\frac{\partial}{\partial x}\left(L\frac{\partial q}{\partial x}\right) + \frac{\partial}{\partial \xi}\left(\Xi_x L\frac{\partial q}{\partial x} + (\Xi_x)^2\frac{\partial q}{\partial \xi}\right) + \frac{\partial^2 q}{\partial \xi^2} \tag{6.3}$$

The extra mixed derivatives that appear in the middle term of eq.(6.3) produce a larger stencil and complicate the calculations, thus reducing the method's computational efficiency. Another problematic feature of this approach is the incorporation of boundary conditions. As it can be seen in eq.(6.1e) the kinematic condition contains both velocity components. This means that the bottom boundary condition for the Poisson equation would take (in conjuction with eq.(6.1a),(6.1b)) the following form:

$$\frac{\partial h}{\partial x}\left(L\frac{\partial q}{\partial x}\right)_{\xi=0} + \left[1+\left(\frac{\partial h}{\partial x}\right)^2\right]\left(\frac{\partial q}{\partial \xi}\right)_{\xi=0} = \left(\frac{\partial h}{\partial x}(Lu)^*_{\xi=0} + (Lw)^*_{\xi=0}\right)/\Delta t \tag{6.4}$$

With the exception of the special case of the flat bottom (where the above is reduced to a Neumann-type condition), such an approach induces numerical difficulties and would be preferable to be avoided.

In order to overcome these two main obstacles we draw inspiration from the Partially Implicit scheme introduced in [62]. The basis of this approach is to incorporate some of the problematic terms of eq.(6.1a),(6.1b) into an explicit step so that those are then absent from the Poisson solver.

Having that in mind and using the notation of $P \overset{\text{def}}{=\!=} Lu$, $Q \overset{\text{def}}{=\!=} Lw$ and the introduction of $\Psi \overset{\text{def}}{=\!=} \Xi_x P + Q$ and $\lambda \overset{\text{def}}{=\!=} \Delta t \cdot q$, the following explicit step is proposed:

$$P' = P^* - \Xi_x \frac{\partial \lambda_{\approx}}{\partial \xi} \tag{6.5a}$$

$$Q' = Q^* - \Xi_x L\frac{\partial \lambda_{\approx}}{\partial x} \tag{6.5b}$$

$$\Psi' \overset{\text{def}}{=\!=} \Xi_x P' + Q' \tag{6.5c}$$

followed by the implicit step of:

$$P = P' - L\frac{\partial \lambda}{\partial x} \tag{6.6a}$$

$$\Psi = \Psi' - \frac{\partial \lambda}{\partial \xi} \tag{6.6b}$$

$$L\frac{\partial P}{\partial x} + \frac{\partial \Psi}{\partial \xi} = 0 \tag{6.6c}$$

$$\text{BC: } \lambda_{\xi=1} = \Psi_{\xi=0} = 0 \tag{6.6d}$$

Something to note is that for calculation of the intermediate field (P', Q') one needs to define the approximate pressure field $\lambda_{\approx} \overset{\text{def}}{=\!=} q_{\approx}\delta t$. For the purposes of the present method the pressure field from the previous timestep will be used. That will be discussed in detail in the next chapter.

Rewritting the divergence-free condition using eq.(6.6) one obtains the following Poisson-like equation:

$$\nabla^2_{\xi}[\lambda] \overset{\text{def}}{=\!=} L\frac{\partial}{\partial x}\left(L\frac{\partial \lambda}{\partial x}\right) + \frac{\partial^2 \lambda}{\partial \xi^2} = L\frac{\partial P'}{\partial x} + \frac{\partial \Psi'}{\partial \xi} \tag{6.7a}$$

$$\text{BC: } \lambda_{\xi=1} = 0 \tag{6.7b}$$

$$\left.\frac{\partial \lambda}{\partial \xi}\right|_{\xi=0} = \Psi'_{\xi=0} \tag{6.7c}$$

The advantages of the new approach are now highlighted: The problematic terms of eq.(6.3) are incorporated into the right hand side of the Poisson-like equation through the intermediate velocity field. Also, by working with the pair (P, Ψ) instead of the (P, Q) the bottom boundary condition is now reduced to a simple Neumann-type one.

An important feature of this approach is that the explicit step of eq.(6.5) scales linearly with the factor Ξ_x. As such, if the layer gradients are sufficiently small, the explicit step does not alter significantly the starting field (i.e. $(P', \Psi') \approx (P, Q)$). That means that the proposed method should be stable in the case of mild layer deformations.

Although eq.(6.7) gives an adequate description of the system that will be discretized, the actual numerical method will be constructed in a fully discrete manner, so that consistency is guarantied.

6.2 Grid staggering

In order to construct the fully discrete VRO scheme, some considerations must be made concerning the distribution of variables on the computational domain. As was described

in §3.5, the variables (L, Lu, Lw) are considered constant on the cells $\Omega_{ij} = [x_i, x_{i+1}] \times [\xi_j, \xi_{j+1}]$:

$$(L, u, w) = (L_{ij}, u_{ij}, w_{ij}) \qquad \text{when: } (x, \xi) \in \Omega_{ij} \tag{6.8}$$

If one approaches the Poisson equation in a standard cell-centered way, the resulting algebraic system is ill-conditioned and the well known erroneous pressure modes appear. In order to bypass those obstacles, the so called *staggered grid* approach is used, where the variables u, w, q are placed in different locations from each other. Grid staggering is a common practice in oceanographic CFD applications, as illustrated by Stelling and Zijlema [63, 64] and more recently in [65] among other sources, because it offers an extremely robust and consistent way to guarantee conservation of mass while maintaining an accurate prediction of the pressure.

In the present method, the standard Arakawa C-grid[1] [67] is used. In the Arakawa C-grid, the horizontal velocity remains on the centre of the cell Ω_{ij}, the vertical one appears in the cell's nodes and the pressure appears in the middle of the vertical cell faces. That configuration alongside the used indexing is presented in Figure 6.1.

6.3 Discrete equations and boundary conditions

Having said that, the discrete form of eq.(6.6) becomes:

$$P_{ij} = P'_{ij} - L_{ij} \frac{\lambda_{i+1,j} - \lambda_{ij}}{\Delta x_i} \tag{6.9a}$$

$$\Psi_{ij} = \Psi'_{ij} - \frac{\lambda_{ij} - \lambda_{i,j-1}}{(l_j + l_{j-1})/2} \tag{6.9b}$$

$$\frac{L_{i-1,j} + L_{ij}}{\Delta x_{i-1} + \Delta x_i} (P_{ij} - P_{i-1,j}) + \frac{\Psi_{i,j+1} - \Psi_{ij}}{l_j} = 0 \tag{6.9c}$$

$$\text{BC: } \lambda_{N_l - 1} + \lambda_{N_l} = 0 \tag{6.9d}$$

$$\Psi_{i0} = 0 \tag{6.9e}$$

$$P_{-1,j} = P^{BC}_{-1,j} \tag{6.9f}$$

$$P_{N_l,j} = P^{BC}_{N_l,j} \tag{6.9g}$$

[1] That type of grid is also proposed in [18] and is referred to as the *2/1 staggered grid* in [66].

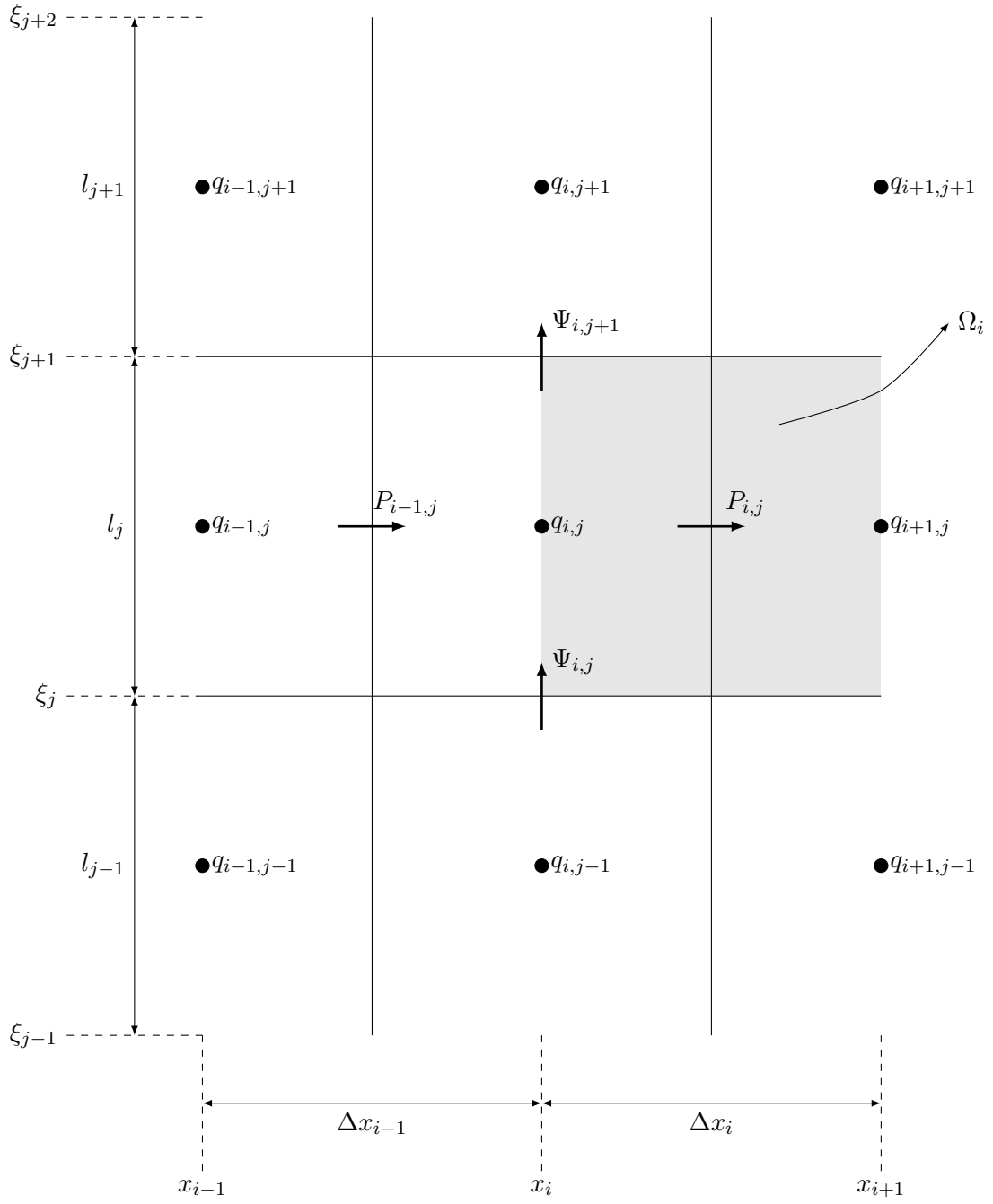

Figure 6.1: Grid staggering technique

After some algebraic manipulations the following set of equations is obtained:

$$\begin{bmatrix} A_{ij}^N \ , \ A_{ij}^E \ , \ -A_{ij} \ , \ A_{ij}^W \ , \ A_{ij}^S \end{bmatrix} \begin{bmatrix} \lambda_{i,j+1} \\ \lambda_{i+1,j} \\ \lambda_{ij} \\ \lambda_{i-1,j} \\ \lambda_{i,j-1} \end{bmatrix} = B_{ij} \quad , \quad \begin{matrix} 0 \leq i \leq N_x \\ 0 \leq j \leq N_l - 1 \end{matrix} \tag{6.10a}$$

$$A_{ij}^N = \frac{2}{l_j(l_{j-1} + l_j)} \tag{6.10b}$$

$$A_{ij}^S = \frac{2}{l_{j-1}(l_{j-1} + l_j)} \tag{6.10c}$$

$$A_{ij}^E = \frac{L_{i,j}(L_{i-1,j} + L_{i,j})}{\Delta x_i(\Delta x_{i-1} + \Delta x_i)} \tag{6.10d}$$

$$A_{ij}^W = \frac{L_{i-1,j}(L_{i-1,j} + L_{i,j})}{\Delta x_{i-1}(\Delta x_{i-1} + \Delta x_i)} \tag{6.10e}$$

$$A_{ij} = A_{ij}^N + A_{ij}^S + A_{ij}^W + A_{ij}^E + \delta_{ij}^{BC} \tag{6.10f}$$

$$B_{ij} = \frac{L_{i-1,j} + L_{ij}}{\Delta x_{i-1} + \Delta x_i} \left(P_{ij}'' - P_{i-1,j}'' \right) + \frac{\Psi_{i,j+1}'' - \Psi_{ij}''}{l_j} = 0 \tag{6.10g}$$

The above equations are in the classic 5-point stencil form of the Finite Difference Poisson equation and thus can be easily solved through a diagonal linear system solver.

When the stencil extends outside the computational boundary, those terms are zeroed and the effects of the boundary conditions are incorporated through the correcting factor δ_{ij}^{BC} in eq.(6.10f).

$$\delta_{ij}^{BC} = \begin{cases} A_{ij}^N & , j = N_l - 1 \\ -A_{ij}^W & , i = 0 \\ -A_{ij}^E & , i = N_x \\ -A_{ij}^S & , j = 0 \\ 0 & , \text{otherwise} \end{cases} \tag{6.11}$$

and the definition of the P'', Ψ'' used on the right hand side of eq.(6.10):

$$P_{ij}'' = \begin{cases} P_{ij}^{BC} & , i = 0, N_x \\ P_{ij}' & , \text{otherwise} \end{cases} \tag{6.12}$$

$$\Psi_{ij}'' = \begin{cases} 0 & , j = 0 \\ \Psi_{ij}' & , \text{otherwise} \end{cases} \tag{6.13}$$

This procedure is written in matrix form in the following way:

$$[\mathbf{PCO}(L)]\,\lambda = \mathbf{div}\left(P', \Psi'; P_{BC}\right) \tag{6.14}$$

6.4 Variable and gradient reconstruction

As it was mentioned, the variables Ψ, q are shifted from their original, cell-centered positions due to the grid staggering technique (see Fig.6.1). The location of the pressure does not effect the numerical procedure, as it is only used within the PCO and thus no contradiction arises. That though is not true for the $\Psi = P\Xi_x + Q$ variable, because the field $(P, Q)^*$ is also used in the other two operators.

In order to obtain those values an averaging procedure is used:

$$\Psi_{ij} = (\Xi_x)_{ij} P_{i-1/2,j-1/2} + Q_{i-1/2,j-1/2} \tag{6.15a}$$

$$\text{with: } P_{i-1/2,j-1/2} = \frac{P_{ij} + P_{i,j-1} + P_{i-1,j} + P_{i-1,j-1}}{4} \tag{6.15b}$$

$$Q_{i-1/2,j-1/2} = \frac{Q_{ij} + Q_{i,j-1} + Q_{i-1,j} + Q_{i-1,j-1}}{4} \tag{6.15c}$$

$$(\Xi_x)_{ij} = (\Xi_x)_{x=x_i}^{\xi=\xi_j} = \frac{-(z_{ij} - z_{i-1,j})}{(\Delta x_i + \Delta x_{i-1})/2} \tag{6.15d}$$

$$z_{ij} = -h_i + \sum_{k=0}^{k<j} l_k L_{ik} \tag{6.15e}$$

The values P_{i,N_l}, Q_{i,N_l} that extend outside the computational domain are obtained through linear extrapolation:

$$(\cdot)_{i,N_l} = 2\left[(\cdot)_{i,N_l-1}\right] - \left[(\cdot)_{i,N_l-2}\right] \tag{6.16}$$

When the PCO procedure is applied, the cell-centered values are retrieved through another averaging:

$$(\cdot)_{ij} = \frac{(\cdot)_{i+1/2,j+1/2} + (\cdot)_{i+1/2,j-1/2} + (\cdot)_{i+1/2,j-1/2} + (\cdot)_{i-1/2,j-1/2}}{4} \tag{6.17}$$

The last thing to address is the discrete form of eq.(6.5) which is chosen to be:

$$P'_{ij} = P^*_{ij} - \Xi^\circ_{ij} \frac{\lambda^{\approx}_{i,j+1} + \lambda^{\approx}_{i+1,j+1} - \lambda^{\approx}_{i,j-1} - \lambda^{\approx}_{i+1,j-1}}{2l_j} \tag{6.18a}$$

$$Q'_{ij} = Q^*_{ij} - \Xi^\circ_{ij} \frac{\lambda^{\approx}_{i+1,j} - \lambda^{\approx}_{i,j}}{\Delta x_i} \tag{6.18b}$$

$$\Xi^\circ_{ij} = \frac{\Xi_x^{i+1,j+1} + \Xi_x^{i,j+1} + \Xi_x^{i+1,j} + \Xi_x^{ij}}{4} \tag{6.18c}$$

6.5 The PCO algorithm

Based on the above PCO procedure can now be outlined:

1. The field (L, P^*, Q^*) and the approximate pressure field $q_{\approx}$ are defined as input.
2. The layer gradient Ξ_x is calculated as per eq.(6.15d).
3. The explicit step of eq.(6.18) is applied upon (P, Q) using the values $q_{\approx}$ to get (P', Q').
4. The eq.(6.15) is used to obtain the nodal values Ψ'_{ij}.
5. The matrices $\mathbf{PCO}(L)$ and $\mathbf{div}(P', \Psi'; P_{BC})$ are calculated through eq.(6.10).
6. The linear system $[\mathbf{PCO}]\,\mathbf{q} = \mathbf{div}$ is solved and the pressure field is obtained.
7. The velocity field is updated through eq.(6.9) thus defining the field (P, Q, q).

The details of this procedure are displayed in Algorithm 5,6.

Algorithm 5 The PCO reconstruction scheme

Input: $L, P^*, Q^*, q_{\approx}, \Delta t, h, L_{BC}, P_{BC}, Q_{BC}$
for $0 \le i \le N_x$ **do**
  $(\Xi_x)_{i0} \leftarrow \dfrac{h_{i+1} - h_i}{\Delta x_i}$
  for $1 \le j \le N_l$ **do**
    $(\Xi_x)_{ij} \leftarrow (\Xi_x)_{i,j-1} - \dfrac{l_{j-1}}{\Delta x_i}\left(L_{i+1,j-1} - L_{i,j-1}\right)$
  end for
end for
$\lambda_{\approx} \leftarrow q_{\approx} \cdot \Delta t$
for $(i,j) \in \{0, N_x - 1\} \times \{0, N_l - 1\}$ **do**
  $\Xi^{\circ}_{ij} \leftarrow \dfrac{\Xi_x^{i+1,j+1} + \Xi_x^{i,j+1} + \Xi_x^{i+1,j} + \Xi_x^{ij}}{4}$
  $P'_{ij} \leftarrow P^*_{ij} - \Xi^{\circ}_{ij} \dfrac{\lambda^{\approx}_{i,j+1} + \lambda^{\approx}_{i+1,j+1} - \lambda^{\approx}_{i,j-1} - \lambda^{\approx}_{i+1,j-1}}{2l_j}$
  $Q'_{ij} \leftarrow Q^*_{ij} - L_{ij}\Xi^{\circ}_{ij} \dfrac{\lambda^{\approx}_{i+1,j} - \lambda^{\approx}_{i,j}}{\Delta x_i}$
end for
for $(i,j) \in \{-1, N_x\} \times \{-1, N_l\}$ **do**
  if $i = -1$ or $i = N_x$ **then**
    $P''_{ij} \leftarrow P^{BC}_{ij}$
    $Q''_{ij} \leftarrow Q^{BC}_{ij}$
  else if $j = N_l$ **then**
    $P''_{ij} \leftarrow 2P'_{i,j-1} - P'_{i,j-2}$
    $Q''_{ij} \leftarrow 2Q'_{i,j-1} - Q'_{i,j-2}$
  else
    $P''_{ij} \leftarrow P'_{ij}$
    $Q''_{ij} \leftarrow Q'_{ij}$
  end if
end for
for $(i,j) \in \{0, N_x\} \times \{0, N_l\}$ **do**
  if $j = 0$ **then**
    $\Psi''_{i0} \leftarrow 0$
  else
    $P''_n \leftarrow \dfrac{P''_{ij} + P''_{i,j-1} + P''_{i-1,j} + P''_{i-1,j-1}}{4}$
    $Q''_n \leftarrow \dfrac{Q''_{ij} + Q''_{i,j-1} + Q''_{i-1,j} + Q''_{i-1,j-1}}{4}$
    $\Psi''_{ij} \leftarrow (\Xi_x)_{ij} P''_n + Q''_n$
  end if
end for
  return $P'', Q'', \Psi'', \Xi_x, \Xi^{\circ}$

Algorithm 6 Discrete PCO scheme

Input: $L, P^*, Q^*, q_{\approx}, h, P_{BC}, Q_{BC}$

The reconstruction process of Algorithm 5 is applied:
$P'', Q'', \Psi'', \Xi_x, \Xi^\circ \leftarrow PCO_{recon}\,(L, P^*, Q^*, q_{\approx}, h, P_{BC}, Q_{BC})$

The matrices $\mathbf{PCO}(L)$ and $\mathbf{div}(P', \Psi'; P_{BC})$ are calculated through eq.(6.10),(6.11).

$\lambda \leftarrow \mathbf{PCO}^{-1}\mathbf{div}$
$q \leftarrow \lambda/\Delta t$

for $(i,j) \in \{0, N_x - 1\} \times \{0, N_l - 1\}$ **do**
$P_{ij} \leftarrow P''_{ij} - L_{ij}\dfrac{\lambda_{i+1,j} - \lambda_{ij}}{\Delta x_i}$
end for

for $(i,j) \in \{0, N_x\} \times \{0, N_l\}$ **do**
$\Psi_{ij} \leftarrow \Psi''_{ij} - \dfrac{\lambda_{ij} - \lambda_{i,j-1}}{(l_j + l_{j-1})/2}$
end for

for $(i,j) \in \{0, N_x - 1\} \times \{0, N_l - 1\}$ **do**
$Q_{ij} \leftarrow \dfrac{\Psi_{i+1,j+1} + \Psi_{i+1,j} + \Psi_{i,j-1} + \Psi_{ij}}{4} - \Xi^\circ_{ij} P_{ij}$
end for
return P, Q, q

Chapter 7

The SLS as a numerical wave tank

In the present chapter the use of the SLS as a numerical wave tank is described. Wave and wave-current generation techniques are discussed and the fully discrete time-marching scheme is presented.

7.1 Boundary conditions and relaxation zones

When dealing with a numerical wave tank, one needs to address the way the boundary conditions are incorporated into the algorithm. The three basic components of the algorithm (mSWE, VRO, PCO) all account for the boundary conditions in the Dirichlet pointwise sense:

$$U_j(a,t) = \left[U^L_{BC}\right]_j(t) \qquad \text{and} \qquad U(b,t) = \left[U^R_{BC}\right]_j(t) \quad , \quad j = 0, ..., N_l - 1 \tag{7.1}$$

where $U = [L, Lu, Lw]^T$.

Although this approach is adequate for simple configurations, when one wants to use the scheme for wave propagation, a technique that also accounts for the horizontal distribution of the target solution must be employed. Although more sophisticated approaches like the Perfectly Matched Layers have been popularized for linear problems [68], their use on nonlinear problems is quite limiting.

In the present method, the standard relaxation zone technique described in [69, 70] is utilized. In this technique the discrete timestepping operator is blended with the enforcement of $\mathcal{R}(U) = (U - U_{zone})/\Delta t = 0$, where $U_{zone}(x,t)$ is the target solution and $m(x)$ a blending function. If the timestepping operator is written in the form $\mathcal{J}(U) =$

$\frac{U-U_0}{\Delta t} + R = 0$, where $U_0 \overset{\text{def}}{=\!=} U(x,t^n)$ the blending takes the form:

$$\begin{aligned}&(1-m)\mathcal{J}(U) + m\mathcal{R}(U) = 0 \Rightarrow \\ \Rightarrow &U = U^* + m\left(U_{zone} - U^*\right)\end{aligned} \tag{7.2}$$

where $U^* = U_0 - \Delta t \cdot R$ the timestepping solution when the blending is ignored.

Again, following [70], the blending function is defined as:

$$m(x) = \frac{\exp\left(\mathcal{X}_{(x)}^p\right) - 1}{\exp(1) - 1} \tag{7.3}$$

$$\mathcal{X}_{(x)} = \begin{cases} \dfrac{L_{in} - (x-a)}{L_{in}} & x \le a + L_{in} \\ 0 & a + L_{in} < x < b - L_{out} \\ \dfrac{L_{out} - (b-x)}{L_{out}} & x \ge b - L_{out} \end{cases} \tag{7.4}$$

with L_{in}, L_{out} being the lengths of the left and right relaxation zones as seen in Fig.7.1. Empirically, the exponent is set to $p = 3.5$.

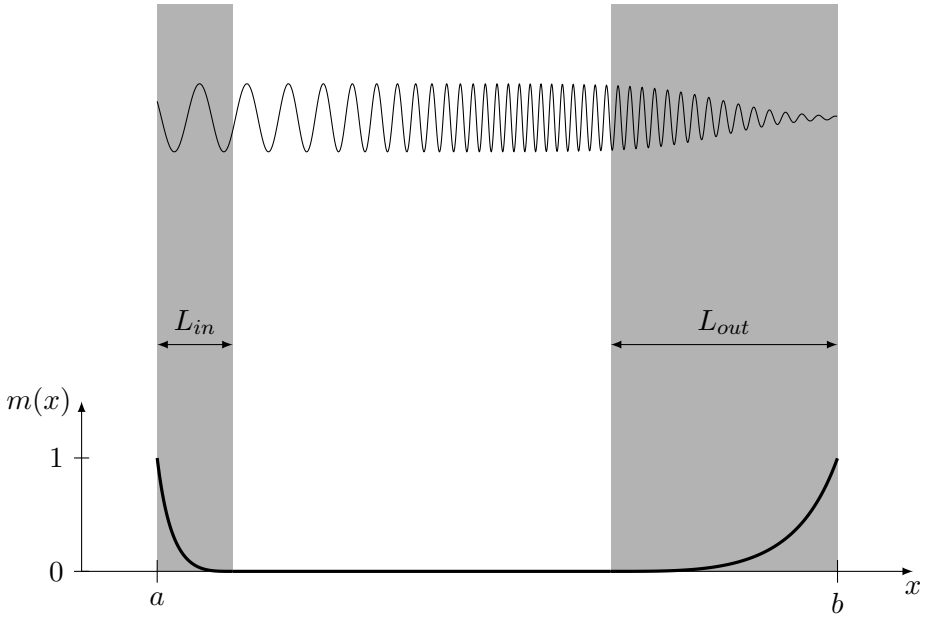

Figure 7.1: Generation/ absorption zones

This procedure allows for an easy implementation of the target solution $U_{zone}(x,t)$ on the timestepping procedure by simply applying eq.(7.5) within each timestep. Even though

one could apply this on each variable L, P, Q separately, in practice the application on only the horizontal discharge $P = Lu$ is sufficient, because that will directly influence the two other variables through the layer kinematics (i.e. the mSWE) and the enforcement of the divergence-free condition (via the PCO). Thus the relaxation scheme takes the form:

$$P_{ij} = P^*_{ij} + m(x^m_i)\left(P^j_{zone}(x^m_i, t) - P^*_{ij}\right) \tag{7.5}$$

where $x^m_i = (x_{i+1} + x_i)/2$.

Note that the pointwise treatment of the boundary conditions within the scheme remains the same and the enforced boundary data are defined through the target solution as:

$$\left[U^L_{BC}(t)\right]_j \leftarrow U^j_{zone}(a, t) \tag{7.6a}$$

$$\left[U^R_{BC}(t)\right]_j \leftarrow U^j_{zone}(b, t) \tag{7.6b}$$

As one may notice, in the above description of the relaxation scheme, both the boundary conditions and the target solution depends on the layer index $0 \leq j < N_l$ in the parametric sense. This is because, depending on the number of layers, a different set of functions $\left\{U^j_{zone}(x, t)\right\}_{j=0}^{j=N_l-1}$ is used, as it will be described in §7.3.

7.2 Stability and timestepping scheme

In order to specify the fully discrete temporal version of the SLS the timestep Δt must be defined in such a way so that the stability of the method is ensured. As it is customary, the influence of the PCO on the stability of the method is considered to be negligible and thus the CFL stability is enforced through eq.(4.37) and eq.(5.10):

$$\Delta t = \mathbb{CFL} \times \min\left\{\left[\min_{ij} \delta^{SWE}_{ij}\right], \left[\min_{ij} \delta^{VRO}_{ij}\right]\right\} \tag{7.7}$$

$$\delta^{SWE}_{ij} = \frac{\Delta x_i}{|P_{ij}/L_{ij}| + \sqrt{gL_{ij}}} \tag{7.8}$$

$$\delta^{VRO}_{ij} = \frac{2l_j L_{ij}}{|\vartheta_{i,j+1} + \vartheta_{ij}|} \tag{7.9}$$

where the parameter $0 < \mathbb{CFL} < 1$ regulates the relative size of the timestep.

After addressing that, the fully discrete time marching scheme can be determined.

1. Given the $\mathbb{CFL}$, the step Δt^n is determined through eq.(7.7) based on the data provided by the previous timestep t^n. The new discrete time is set as $t^{n+1`} = t^n + \Delta t^n$.

2. The pointwise boundary data that will be passed to the mSWE,PCO are calculated based on the target solution by using eq.(7.6) at $t = t^n$.

3. The mSWE (Algorithm 3) is applied on U^n to obtain the intermediate values $U^{(1)}$.

4. The relaxation zone technique is applied on $P^{(1)}$ through eq.(7.5) to obtain $P^{(2)}$

5. The VRO (Algorithm 4) is applied on $U^{(2)}$ to obtain the remeshed field $U^{(3)}$ and the ϑ^{n+1}.

6. The PCO (Algorithm 6) is applied on $U^{(3)}$ and the final field U^{n+1}, q^{n+1} is thus calculated. The approximate pressure field used in the partially implicit approach of eq.(6.5) is set equal to q^n, that is known from the previous timestep.

as usual the notation $U = [L, P, Q]^T = [L, Lu, Lw]^T$ is used. The procedure is also described in Algorithm 7.

Algorithm 7 The discrete SLS

Input: $U^0, q^0, h_i, x_i, l_j, \mathbb{CFL}, m(x), U^j_{zone}(x,t)$

for $1 \leq n < N_t$ **do**

$$\delta^{SWE} \leftarrow \min_{ij} \left\{ \frac{\Delta x_i}{\left| P^{n-1}_{ij} / L^{n-1}_{ij} \right| + \sqrt{g L_{ij}}} \right\}$$

$$\delta^{VRO} \leftarrow \min_{ij} \left\{ \frac{2 l_j L^{n-1}_{ij}}{\left| \vartheta^{n-1}_{i,j+1} + \vartheta^{n-1}_{ij} \right|} \right\}$$

$$\Delta t \leftarrow \mathbb{CFL} \times \min \left\{ \delta^{SWE}, \delta^{VRO} \right\}$$
$$t^n \leftarrow t^{n-1} + \Delta t$$

$$\left[U^L_{BC} \right]_j \leftarrow U^j_{zone} \left(x_0, t^n \right)$$
$$\left[U^R_{BC} \right]_j \leftarrow U^j_{zone} \left(x_{N_x}, t^n \right)$$

The Multilayer Shallow Water Equations (Algorithm 3) are solved:
$$U^* \leftarrow mSWE \left(U^{n-1}, \Delta t, h_i, U^{L/R}_{BC} \right)$$

The relaxation zone technique eq.(7.5) is applied on the horizontal velocity:
$$P^*_{ij} \leftarrow P^*_{ij} + m(x^m_i) \times \left(P^j_{zone}(x^m_i, t^n) - P^*_{ij} \right)$$

The Vertical Remeshing Operator (Algorithm 4) is applied:
$$U^*, \vartheta^n \leftarrow VRO \left(U^*, \Delta t \right)$$

The Pressure Correction Operator (Algorithm 6) is applied:
$$U^n, q^n \leftarrow PCO \left(U^*, q^{n-1}, \Delta t, U^{L/R}_{BC} \right)$$

end for

return L, P, Q, q, t

7.3 Dispersion properties and wave/current propagation

7.3.1 Irrotational waves

In order to address the topic of wave propagation let us consider a wave of small amplitude A_η propagating over a bottom of constant depth h. According to the linear theory of Airy [71, §2.1], if the wave is of sinusoidal nature with length λ, propagating with speed c, the field is described by:

$$\eta(x,t) = A_\eta \times \cos\left[k(x-ct)\right] \tag{7.10a}$$
$$u(x,\sigma,t) = A_u \times \cosh\left[kh\sigma\right] \times \cos\left[k(x-ct)\right] \tag{7.10b}$$
$$w(x,\sigma,t) = A_u \times \sinh\left[kh\sigma\right] \times \sin\left[k(x-ct)\right] \tag{7.10c}$$
$$\text{with: } A_u = ckA_\eta/\sinh kh \tag{7.10d}$$

The vertical coordinate is defined as $\sigma = (z+h)/h$ and the wave number as $k = 2\pi/\lambda$. The wave celerity is calculated using the classic dispersion relation for linear waves:

$$\frac{c_{Airy}^2}{gh} = \frac{\tanh kh}{kh} \tag{7.11}$$

In order to test the performance of the layer-discrete SLS with respect to propagation, the method to calculate the dispersion relation of the semi-discrete linearized system is presented in Appendix C. Following that, the dispersion relations are analytically calculated:

$$\frac{c^2}{gh} = \frac{2}{kh^2+2} \qquad N_l = 1 \tag{7.12a}$$
$$= \frac{4kh^2+32}{kh^4+16kh^2+32} \qquad N_l = 2 \tag{7.12b}$$
$$= \frac{6kh^4+216kh^4+1458}{kh^6+54kh^4+729kh^2+1458} \qquad N_l = 3 \tag{7.12c}$$
$$= \frac{\sum_{n=0}^{N-1}\alpha_n(kh)^{2n}}{\sum_{k=0}^{N}\beta_k(kh)^{2k}} \qquad N_l = N \tag{7.12d}$$

Those dispersion relations of the layer-discrete systems are compared with eq.(7.11) in Figures 7.2,7.3. It is observed that as the number of layers increases, the dispersion relation tends to coincide with the analytic one. That indicates that with the addition of layers, the dispersion properties of the model are enhanced and thus waves of shorter length can be accurately simulated.

Another thing to note is that the difference between the discrete dispersion relation and the analytical one stems from the fact that eq.(C.7) is a discretization of the Helmholtz equation:

$$\frac{\partial^2 q^*}{\partial \sigma^2} - (kh)^2 q^* = (kh)^2 \quad \text{with:} \quad \left.\frac{\partial q^*}{\partial \sigma}\right|_{\sigma=0} = q^*|_{\sigma=1} = 0 \qquad \sigma \in [0,1] \tag{7.13}$$

That equation's analytic solution is $q^*_{th} = \dfrac{\cosh(kh\sigma)}{\cosh kh} - 1$. That, when substituted into eq.(C.9), gives the analytic dispersion relation of the Airy theory. This means that the dispersion error is essentially the error related to the discretization of eq.(7.13).

7.3.2 Current incorporation and boundary data

When dealing with waves propagating on top of a current, dispersion relations become complicated, because the solution of the Rayleigh equation is required in order to calculate them. Thus, approximate methods are abundant in the literature.

Let $V(\sigma)$ be a vertical current profile and $\widetilde{V} = V(1)$ its free surface trace. For the purposes of defining the boundary conditions of the method, the following approximate relation is used [72]:

$$c_{\approx} = \widetilde{V} + \left[\sqrt{(c_0)^2 + \delta^2} - \delta\right] \tag{7.14}$$

$$\text{with : } \delta = \delta[V'] = \int_0^1 V'(\sigma)\frac{\sinh(2kh\sigma)}{\sinh(2kh)}d\sigma \tag{7.15}$$

Where c_0 denotes the celerity in the absence of the current, calculated by eq.(7.11).

If the background flow is considered to be piecewise constant V_i in a mesh $[\sigma_i, \sigma_{i+1}]$, the relation can be rewritten as:

$$c_{\approx} = \sqrt{(c_0)^2 + (\delta_* - V_{N-1})^2} + \delta_* \tag{7.16}$$

$$\text{with : } \delta_* = \delta_*[V_j] = \sum_{j=0}^{N_l - 1} V_j(N_{j+1} - N_j) \tag{7.17}$$

$$N_j = \frac{\sinh(2kh\sigma_j)}{\sinh(2kh)} \tag{7.18}$$

Having said that, the travelling wave solution that will be used for wave and wave-current generation is defined through eq.(7.10). If the wavenumber k, the amplitude A_η,

the depth h and the current V_j are known, those equations written in a layerwise manner are:

$$H_{wc}(x,t) = h + A_\eta \times \cos\left[k(x - c_{\approx}t)\right] \tag{7.19a}$$

$$u^j_{wc}(x,t) = V_j + A_u \times \cosh_j \times \cos\left[k(x - c_{\approx}t)\right] \quad , \; j = 0, ..., N_l - 1 \tag{7.19b}$$

$$w^j_{wc}(x,t) = A_u \times \sinh_j \times \sin\left[k(x - c_{\approx}t)\right] \quad , \; j = 0, ..., N_l - 1 \tag{7.19c}$$

$$A_u = c_{\approx} k A_\eta / \sinh kh \tag{7.19d}$$

The celerity is $c_{\approx}$ is calculated trough eq.(7.16). The celerity c_0 is considered to be equal to that of the Airy wave theory. The hyperbolic functions are averaged in the following manner:

$$\cosh_j = \frac{1}{\sigma_{j+1} - \sigma_j} \int_{\sigma_j}^{\sigma_{j+1}} \cosh(kh\sigma) d\sigma = \frac{\sinh(kh\sigma_{j+1}) - \sinh(kh\sigma_j)}{kh\sigma_{j+1} - kh\sigma_j} \tag{7.20}$$

$$\sinh_j = \frac{1}{\sigma_{j+1} - \sigma_j} \int_{\sigma_j}^{\sigma_{j+1}} \sinh(kh\sigma) d\sigma = \frac{\cosh(kh\sigma_{j+1}) - \cosh(kh\sigma_j)}{kh\sigma_{j+1} - kh\sigma_j} \tag{7.21}$$

When the set of eq.(7.19) will be used in the relaxation zone scheme for wave generations, the following restrictions must be noted:

- The wave amplitude must be small enough in order for the Airy theory to be applicable.
- The 3 main conditions as noted in [72] (weak current, weak shear or short wavelength) must be somehow met so that the approximation of eq.(7.16) is accurate enough.
- The number of layers must be large enough so that the celerity of the discrete system remains close to the analytic solution to the Airy theory. One way to estimate that is the dispersion analysis of the previous section.

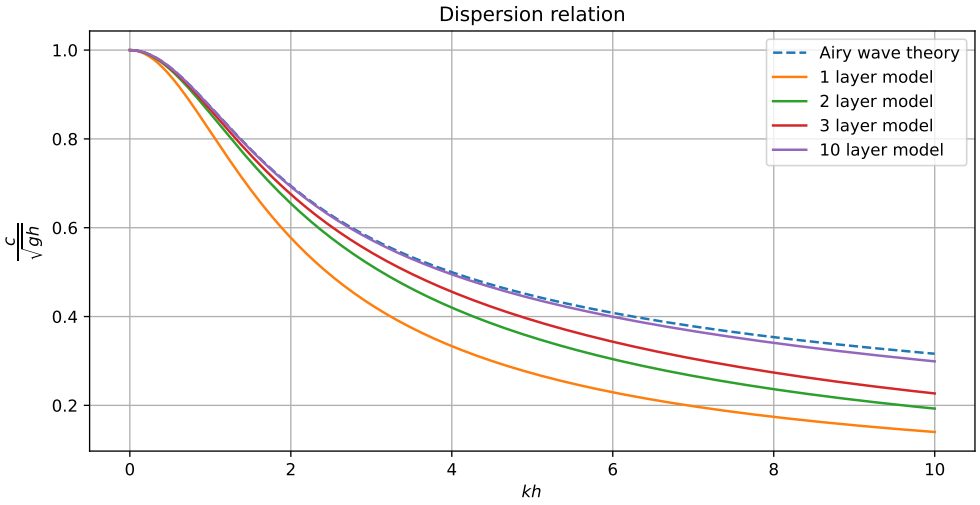

Figure 7.2: Dispersion relation curves

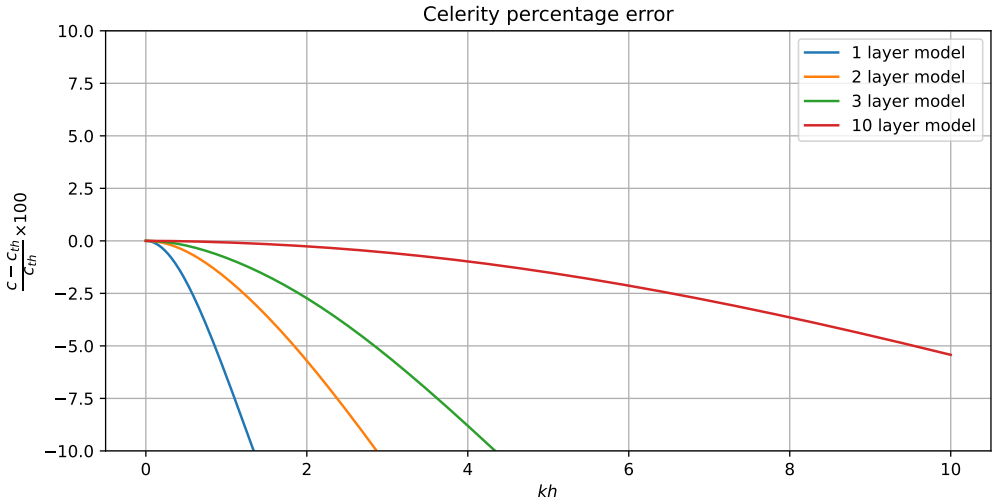

Figure 7.3: Celerity error curves

Chapter 8

Numerical results

8.1 Propagation over submerged trapezoid

In order to test the model's ability to simulate the propagation of waves over general bathymetry, the well-known experiment of [73] is used.

In the long wave case, a sinusoidal wave of length $\lambda = 3.7407m$ and amplitude $A = 0.01m$ propagates over a varying topography with $0.1 \leq h \leq 0.4$.

Concerning the discretization, the horizontal domain $x \in [-10, 40]$ is divided into $N_x = 3000$ cells of equal size. On the vertical direction, $N_l = 10$ layers are used and $l_j = 1/N_l$ is set. In order to marginally ensure stability, $\mathbb{CFL} = 0.9$ is chosen.

Wave generation/absorption is performed by the relaxation zone technique using eq.(7.19), with $L_{in} = L_{out} = 3\lambda$. In order to gradually introduce the wave, the amplitude is set to vary with time: $A_\eta = A \tanh(t/\tau)$, where $\tau = 4\lambda/\left(g \times h_{max}\right)^{1/2}$.

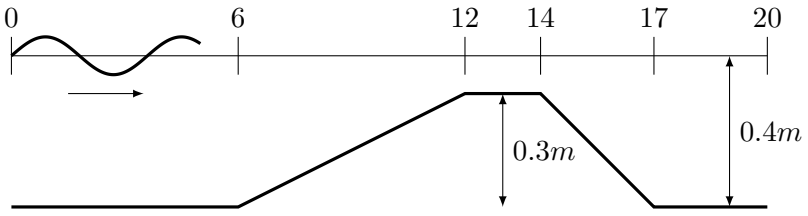

Figure 8.1: The immersed trapezoid setup

The resulting field (P, Q, q) at $t = 58.96s$ is presented in Figures 8.2, 8.3 and 8.4. The timeseries of the free surface elevation alongside the experimental data at the various

stations are presented in Fig.8.5.

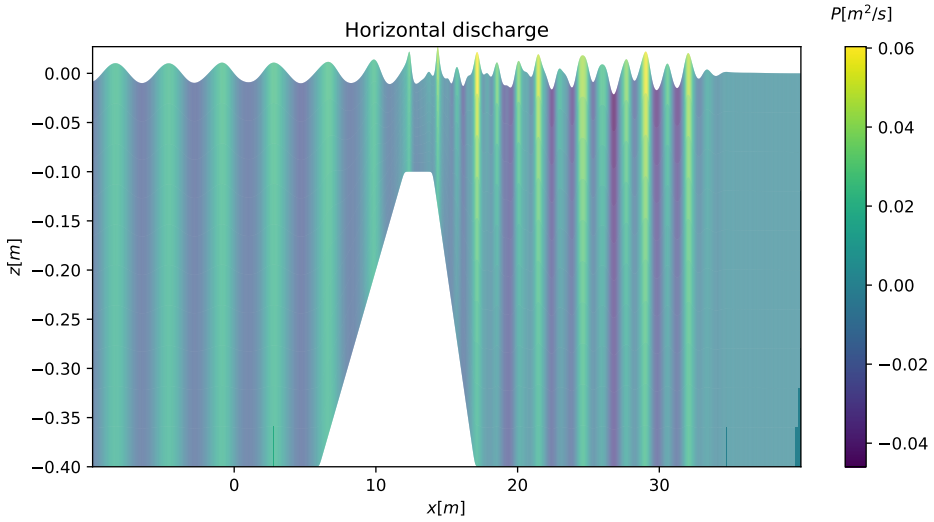

Figure 8.2: Submerged trapezoid, P field

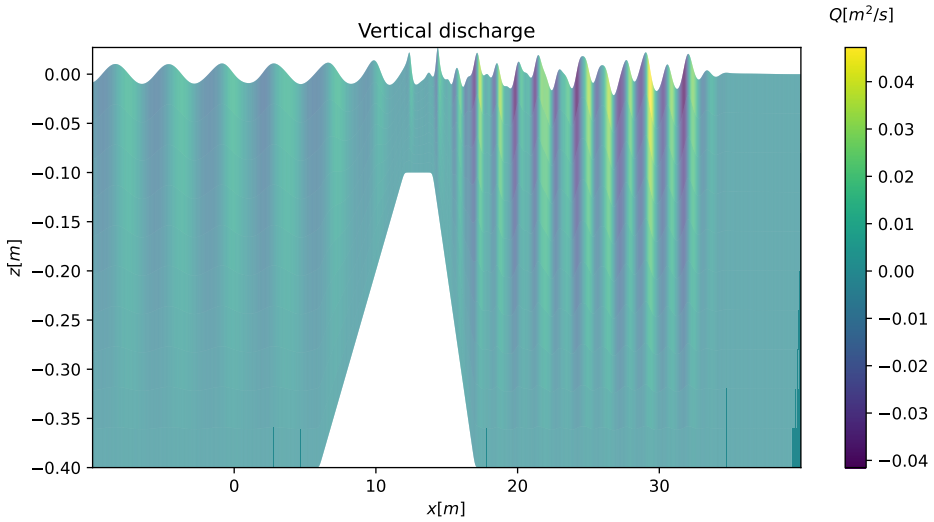

Figure 8.3: Submerged trapezoid, Q field

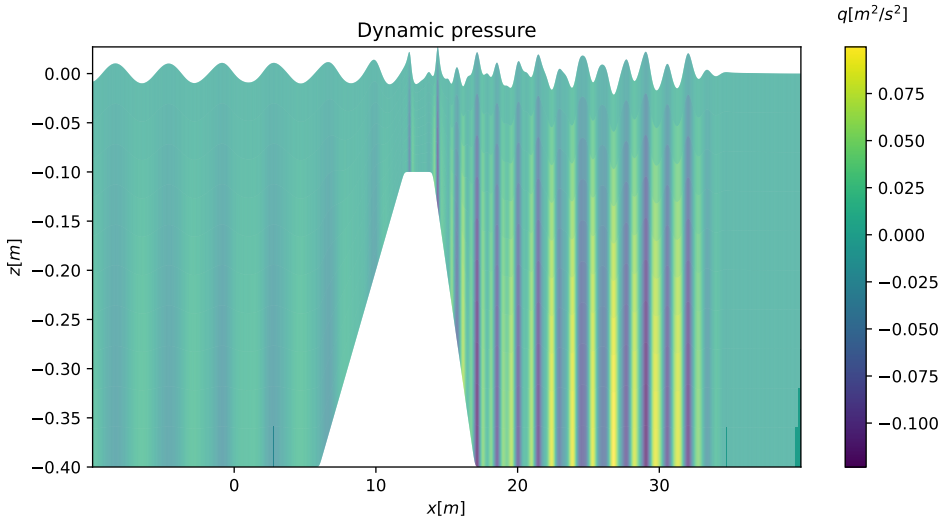

Figure 8.4: Submerged trapezoid, q field

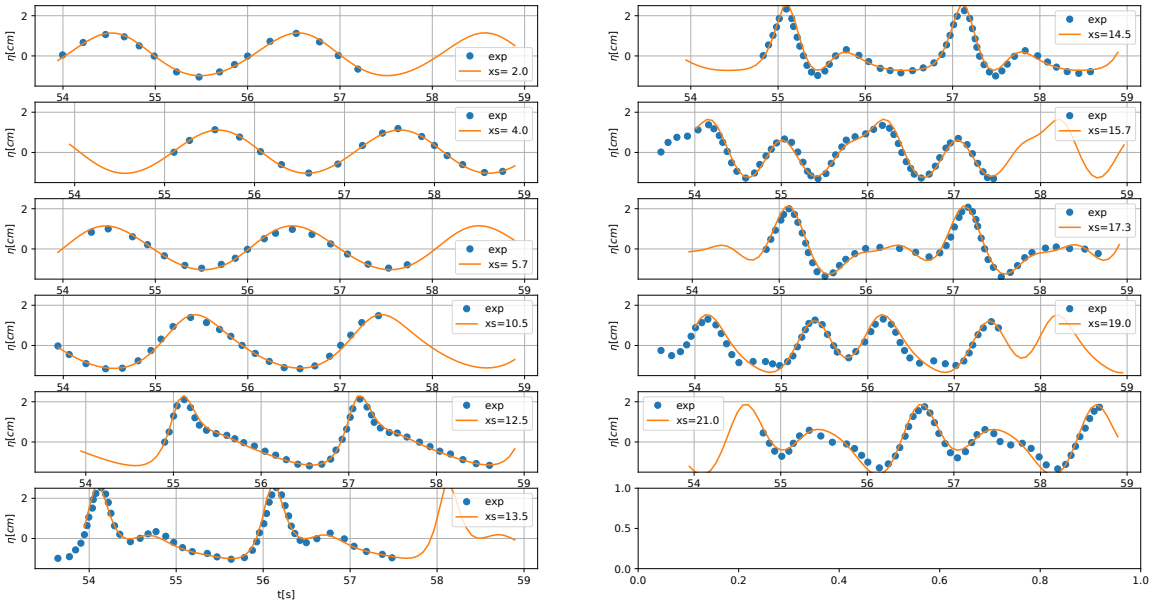

Figure 8.5: Free surface elevation at stations

The results validate the performance of the model, since the wave transformation is captured in a robust manner. Specifically, as it is shown in Fig.8.5, the simulated free surface elevation remains really close to the experimental data even at the last stations, where it is known that the dispersion effects are dominant. Small differences appear at the last two stations, but are considered acceptable. Those results show that the SLS is able, with a reasonable number of layers ($N_l = 10$), to capture dispersion phenomena of non-trivial nature, even in the presence of varying bottom topography.

8.2 Wave-current interaction

In order to test the SLS in the wave-current interaction cases, the following set of simulations is performed. Linear waves of amplitude $A_\eta = 0.001(h/0.4)$ and length $\lambda = 5m$ propagate on top of a bottom of constant depth h in the present of a shear current. Two current configurations (linear,exponential) are considered: $Fr_{lin} = 0.1\sigma$ and $Fr_{exp} = 0.1\exp[3(\sigma - 1)]$. In order to alter the value of kh, a discrete set of depths are simulated separately: $h[m] = \{0.4, 0.8, 1.6, 4\}$.

Regarding the discretization, the horizontal domain $x \in [0, 100]$ is divided into $N_x = 2000$ cells of equal size. On the vertical direction, $N_l = 10$ layers are used with $l_j = 1/N_l$. Concerning the timestepping, $\mathbb{CFL} = 0.5$ is chosen.

Wave generation is performed by the relaxation zone technique using eq.(7.19), with $L_{in} = L_{out} = 3\lambda$. In order to gradually introduce the wave, the amplitude is set to vary with time: $A_\eta = A\tanh(t/\tau)$, where $\tau = 4\lambda/(g \times h_{max})^{1/2}$. The current flow is used as the initial condition.

The resulting curves in the absence of background flow and with linear/exponential current profiles are presented in Figures 8.6, 8.7 and 8.8 respectively. Alongside the simulation results, the analytic curves calculated through eq.(7.14) are plotted. Note that the wave nonlinearity is kept low ($A/h = 0.25\%$), so that those relations are applicable.

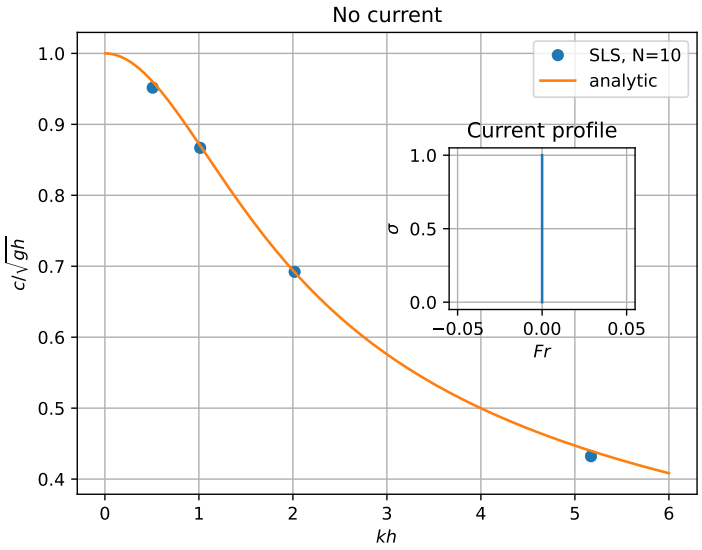

Figure 8.6: No current

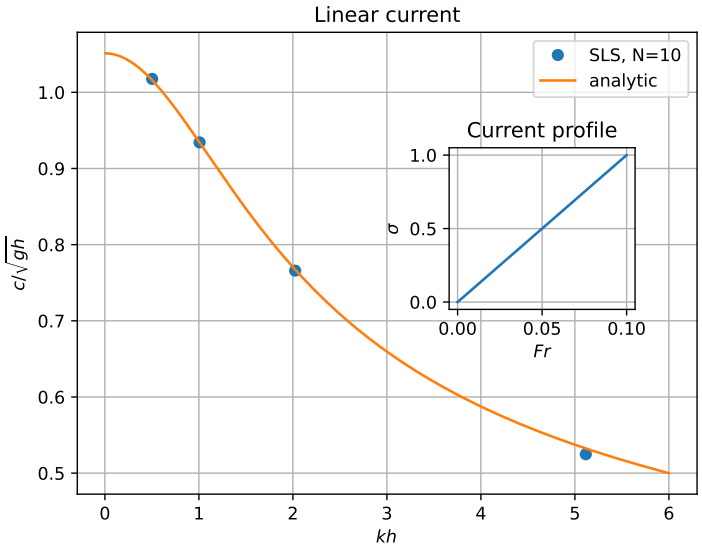

Figure 8.7: Linear current profile

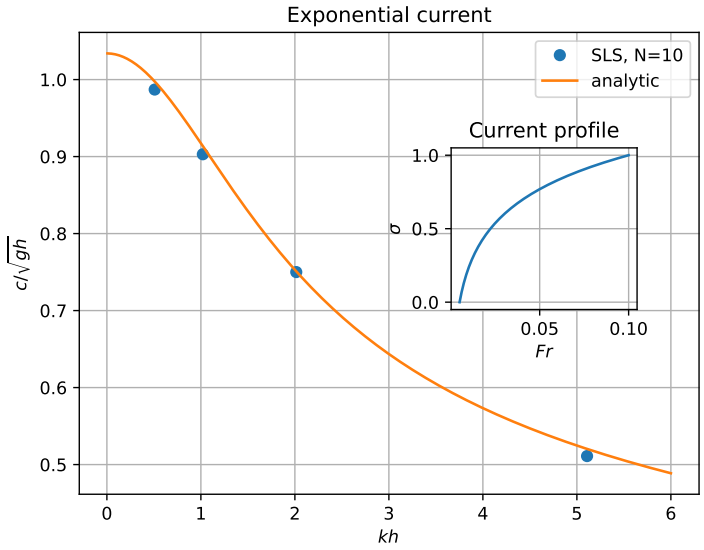

Figure 8.8: Exponential current profile

The simulated wave celerities are extremely close to the analytic curves and thus the ability of the SLS to simulate the propagation of waves on top of currents of arbitrary shear is demonstrated.

Chapter 9

Concluding remarks

9.1 Brief summary

In the present thesis a numerical scheme for the Free-Surface Euler system in general bathymetry is presented. The σ-coordinate transformation is generalized in a layer-wise manner and the Generalized-Coordinate Euler system (GCE) is proposed. The system is treated by a standard operator splitting technique with the addition of a layer kinematic scheme. The mathematical modeling is done in such a way so that the horizontal advection is performed through the Multilayer Shallow Water Equations (mSWE), followed by the proposed Vertical Remeshing Operator (VRO) and the standard Pressure Correction Operator (PCO). Those three operators constitute the Semi-Lagrangian Splitting scheme (SLS).

Following the literature, a standard second-order Finite Volume scheme is designed for the numerical resolution of the mSWE. A remeshing strategy is employed through the VRO so that the well-known loss of hyperbolicity in the mSWE does not become prevalent. The VRO is solved through a simple one-wave Finite Volume scheme. The pressure coupling is performed through the PCO by a partially implicit approach, followed by the solution of a Poisson-like equation on a staggered grid in a standard Finite Difference manner.

The dispersive properties of the linearized SLS are analyzed and boundary conditions for wave propagation (with and without the presence of current) are proposed. The method's performance is tested on the wave propagation over variable bathymetry and in the wave-current interaction over a flat bottom cases. Comparison with experimental results and analytic relations show good agreement, thus verifying the method's accuracy.

9.2 Directions for future research

As an epilogue some possible directions for future research are outlined:

- Numerical investigation of more severe nonlinear wave phenomena in order to test the model's limits/capabilities.
- Enrichment of the model with additional physical considerations, like: variable density (stratified flows), effects of viscosity e.t.c.
- Investigation of how the layers' placement influences the dispersive characteristics of the system. A starting point could be an error analysis of eq.(7.13) on various grids.
- Extension of the model to 3 dimensions. In that case, the splitting technique that constitutes the core of the SLS is expected to remain the same, but a 2D SWE solver and a 3D Poisson solver would need to be constructed.

Concerning the possible extension of the present model for large-scale oceanographic applications, a -quite optimistic- quote from [37, §6.3] is cited:

> *[...] We thus conjecture that it is only a matter of time before we see a vertical Lagrangian-remap-based nonhydrostatic ocean dynamical core for realistic global and regional applications.*

Appendix A

Generalized Vertical Coordinates

In the present appendix, the notion of coordinate transformation is generalized. Let us now consider a mapping of the type $(x', z', t') \mapsto (x, z, t)$ with:

$$x = x' \tag{A.1a}$$
$$z = \mathcal{P}(x', z', t') \tag{A.1b}$$
$$t = t' \tag{A.1c}$$

The function $\mathcal{P}$ is kept arbitrary.

According to the chain rule, the derivatives are:

$$\frac{\partial f}{\partial t'} = \frac{\partial f}{\partial t} + \frac{\partial \mathcal{P}}{\partial t'}\frac{\partial f}{\partial z} \tag{A.2a}$$
$$\frac{\partial f}{\partial x'} = \frac{\partial f}{\partial x} + \frac{\partial \mathcal{P}}{\partial x'}\frac{\partial f}{\partial z} \tag{A.2b}$$
$$\frac{\partial f}{\partial z'} = \frac{\partial \mathcal{P}}{\partial z'}\frac{\partial f}{\partial z} \tag{A.2c}$$

Before we proceed further, the following quantities are defined:

$$\mathcal{T} \overset{\text{def}}{=\!=} -\frac{\partial \mathcal{P}}{\partial t'} \tag{A.3a}$$
$$\mathcal{X} \overset{\text{def}}{=\!=} -\frac{\partial \mathcal{P}}{\partial x'} \tag{A.3b}$$
$$\mathcal{C} \overset{\text{def}}{=\!=} \frac{\partial \mathcal{P}}{\partial z'} \tag{A.3c}$$

Multiplying eq.(A.2) with $\mathcal{C}$ the following relations are produced:

$$\mathcal{C}\frac{\partial f}{\partial t} = \mathcal{C}\frac{\partial f}{\partial t'} + \mathcal{T}\frac{\partial f}{\partial z'} \tag{A.4a}$$

$$\mathcal{C}\frac{\partial f}{\partial x} = \mathcal{C}\frac{\partial f}{\partial x'} + \mathcal{X}\frac{\partial f}{\partial z'} \tag{A.4b}$$

$$\mathcal{C}\frac{\partial f}{\partial z} = \frac{\partial f}{\partial z'} \tag{A.4c}$$

And then by noticing that $\frac{\partial \mathcal{C}}{\partial t'} = \frac{\partial^2 \mathcal{P}}{\partial z' \partial t'} = -\frac{\partial \mathcal{T}}{\partial z'}$ and $\frac{\partial \mathcal{C}}{\partial x'} = \frac{\partial^2 \mathcal{P}}{\partial z' \partial x'} = -\frac{\partial \mathcal{X}}{\partial z'}$, eq.(A.4) are written in the alternative "conservative" form:

$$\mathcal{C}\frac{\partial f}{\partial t} = \frac{\partial}{\partial t'}(\mathcal{C}f) + \frac{\partial}{\partial z'}(\mathcal{T}f) \tag{A.5a}$$

$$\mathcal{C}\frac{\partial f}{\partial x} = \frac{\partial}{\partial x'}(\mathcal{C}f) + \frac{\partial}{\partial z'}(\mathcal{X}f) \tag{A.5b}$$

$$\mathcal{C}\frac{\partial f}{\partial z} = \frac{\partial f}{\partial z'} \tag{A.5c}$$

Similar expressions appear in the literature of moving grids, where $\mathcal{C}$ is referred to as the capacity function [74].

If now the velocity field u, w is introduced, the material derivative takes the form:

$$\mathcal{C}\frac{Df}{Dt} = \frac{\partial}{\partial t'}(\mathcal{C}f) + \frac{\partial}{\partial x'}(\mathcal{C}uf) + \frac{\partial}{\partial z'}(\mathcal{W}f) \tag{A.6}$$

$$\text{where: } \mathcal{W} \overset{\text{def}}{=\!=} w + u\mathcal{X} + \mathcal{T} \tag{A.7}$$

Furthermore, if the mapping is of the type $[0,1] \overset{\mathcal{P}}{\mapsto} [-h, \eta]$, the FSE, as described by the set of eq.(2.5), can be rewritten using the set of eq.(A.5):

$$\frac{\partial}{\partial x'}(\mathcal{C}u) + \frac{\partial}{\partial z'}(w + u\mathcal{X}) = 0 \tag{A.8a}$$

$$\frac{\partial}{\partial t'}(\mathcal{C}u) + \frac{\partial}{\partial x'}\left(\mathcal{C}u^2 + \frac{1}{2}g\mathcal{C}^2 + \mathcal{C}q\right) + \frac{\partial}{\partial z'}(\mathcal{W}u + \mathcal{X}q) = g\mathcal{C}\frac{\partial}{\partial x'}(\mathcal{C} - \eta) \tag{A.8b}$$

$$\frac{\partial}{\partial t'}(\mathcal{C}w) + \frac{\partial}{\partial x'}(\mathcal{C}uw) + \frac{\partial}{\partial z'}(\mathcal{W}w + q) = 0 \tag{A.8c}$$

$$\text{BC: } \mathcal{W}_{z'=0} = \mathcal{W}_{z'=1} = q_{z'=1} = 0 \tag{A.8d}$$

Note that the SCE of eq.(2.17) and the GCE of eq.(3.12) are derived as special cases of this system when one defines:

$$z' = \sigma \quad \Longrightarrow \quad \mathcal{P} = -h + \sigma H \tag{A.9}$$

$$z' = \xi \quad \Longrightarrow \quad \mathcal{P} = \mathcal{P}_\Xi(x', \xi, t') \tag{A.10}$$

Appendix B

The two-layer SWE

Consider the two-layer ($N_l = 2$) version of the mSWE system in its eq.(4.1) form, with $l_1 = l_2 = \frac{1}{2}$. This system is written as:

$$\frac{\partial}{\partial t}(L_1) + \frac{\partial}{\partial x}(L_1 u_1) = 0 \tag{B.1a}$$

$$\frac{\partial}{\partial t}(L_1 u_1) + \frac{\partial}{\partial x}\left(L_1 u_1^2\right) + g L_1 \frac{\partial}{\partial x}\left(\frac{L_1 + L_2}{2}\right) = g L_1 \frac{\partial h}{\partial x} \tag{B.1b}$$

$$\frac{\partial}{\partial t}(L_2) + \frac{\partial}{\partial x}(L_2 u_2) = 0 \tag{B.1c}$$

$$\frac{\partial}{\partial t}(L_2 u_2) + \frac{\partial}{\partial x}\left(L_2 u_2^2\right) + g L_2 \frac{\partial}{\partial x}\left(\frac{L_1 + L_2}{2}\right) = g L_2 \frac{\partial h}{\partial x} \tag{B.1d}$$

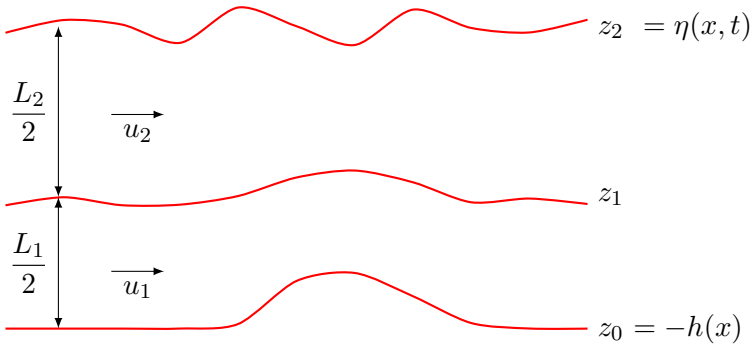

Figure B.1: The two-layer SWE

or in the quasi-linear form:

$$\frac{\partial \mathbf{U}}{\partial t} + \mathbf{A}(\mathbf{U})\frac{\partial \mathbf{U}}{\partial x} = \mathbf{S}(\mathbf{U};h) \tag{B.2a}$$

$$\text{where: } \mathbf{A}(\mathbf{U}) = \begin{bmatrix} 0 & 1 & 0 & 0 \\ (c_1)^2 - (u_1)^2 & 2u_1 & (c_1)^2 & 0 \\ 0 & 0 & 0 & 1 \\ (c_2)^2 & 0 & (c_2)^2 - (u_2)^2 & 2u_2 \end{bmatrix} \tag{B.2b}$$

$$\mathbf{S}(\mathbf{U};h) = \begin{bmatrix} 0 \ , & gL_1\dfrac{\partial h}{\partial x} \ , & 0 \ , & gL_2\dfrac{\partial h}{\partial x} \end{bmatrix}^T \tag{B.2c}$$

$$\text{and: } \mathbf{U} \overset{\text{def}}{=\!=} \begin{bmatrix} L_1 \ , & L_1u_1 \ , & L_2 \ , & L_2u_2 \end{bmatrix}^T \tag{B.2d}$$

$$c_j \overset{\text{def}}{=\!=} \sqrt{\frac{gL_j}{2}} \quad , \quad j = 1,2 \tag{B.2e}$$

As pointed out in the literature [49, 75, 76], the two-layer system's eigenvalues cannot be analytically calculated and may even be complex. In the special case of equal layer heights $L_1 = L_2 = H$, the eigenvalues of the system can be explicitly expressed [77]. By setting $c \overset{\text{def}}{=\!=} \sqrt{gH}$ those are:

$$\lambda_{1,2,3,4} = eig(\mathbf{A}) = \frac{u_1+u_2}{2} \pm \frac{1}{2}\sqrt{2c^2 + (u_2-u_1)^2 \mp 2c\sqrt{c^2 + 2(u_2-u_1)^2}} \tag{B.3}$$

$$= \overline{u} \pm \frac{c}{2}\sqrt{2 + \delta^2 \mp 2\sqrt{1+2\delta^2}} \tag{B.4}$$

where $\delta \overset{\text{def}}{=\!=} \dfrac{|u_2-u_1|}{c}$, $\overline{u} = \dfrac{u_2+u_1}{2}$ and $\pm, \mp$ switch signs independently.

It is then observed that in the (very relevant) case of $0 < \delta < 2$, two of those eigenvalues become complex and thus hyperbolicity is lost. Note that in the case of equal velocities ($\delta = 0$), those eigenvalues are consistent with those of the regular one-layer system: $\lambda_{1,2} = u \pm c$ and $\lambda_{3,4} = 0$.

Appendix C

Discrete dispersion relation

Let us consider a small free surface perturbation (i.e. $\eta/h \ll 1$) over a horizontal bottom with $h = const$. Aiming to linearize the system, the convection terms $Lu^2, Luw, \vartheta u, \vartheta w$ are omitted from the SLS in eq.(3.39),(3.40). Considering the PCO, $\Xi_x \ll 1$ is assumed. This means that eq.(6.5) vanish and in eq.(6.6) $\Psi \approx hw$. Based on that and using the staggering formulation of the PCO described in §6.2 and eq.(6.9), the linearized version of the semi-discrete SLS is formed. Considering a uniform spacing of $l_j = 1/N$, this is written as:

$$\frac{\partial \eta}{\partial t} + \frac{h}{N}\frac{\partial}{\partial x}\sum_{j=0}^{j<N} u_j = 0 \tag{C.1}$$

$$\frac{\partial u_j}{\partial t} + g\frac{\partial \eta}{\partial x} + \frac{\partial q_j}{\partial x} = 0 \qquad j = 0, ..., N-1 \tag{C.2}$$

$$\frac{\partial w_j}{\partial t} + \frac{q_j - q_{j-1}}{h/N} = 0 \qquad j = 0, ..., N \tag{C.3}$$

$$\frac{\partial u_j}{\partial x} + \frac{w_{j+1} - w_j}{h/N} = 0 \qquad j = 0, ..., N-1 \tag{C.4}$$

$$\text{BC:} \qquad q_N + q_{N-1} = 0 \qquad \text{and} \qquad q_0 - q_{-1} = 0 \tag{C.5}$$

Substituting the momentum equations into the continuity we obtain the Poisson-like equation for the pressure:

$$\frac{\partial^2 q_j}{\partial x^2} + \frac{q_{j+1} - 2q_j + q_{j-1}}{(h/N)^2} = -g\frac{\partial^2 \eta}{\partial x^2} \tag{C.6}$$

Now, let us use the frequency domain using the complex representation $f(x,t) = \Re\left\{\mathring{f}\exp\left[ik(x-ct)\right]\right\}$ where $\mathring{f} \in \mathbb{C}$.

The Poisson equation now becomes:

$$(ik)^2\mathring{q}_j + \frac{\mathring{q}_{j+1} - 2\mathring{q}_j + \mathring{q}_{j-1}}{(h/N)^2} = -g(ik)^2\mathring{\eta} \tag{C.7}$$

Setting $\mathring{\eta} = A \in \mathbb{R}$ and $q^* \overset{\text{def}}{=\!=} \dfrac{\mathring{q}}{gA}$ the following linear system can be formulated:

$$\mathcal{A}q^* = \begin{bmatrix} -1 & 1 & & & & & & \\ a & 1-2a & a & & & & & \\ & a & 1-2a & a & & & & \\ & & \ddots & \ddots & \ddots & & & \\ & & & a & 1-2a & a & & \\ & & & & a & 1-2a & a & \\ & & & & & 1 & 1 \end{bmatrix} \begin{bmatrix} q^*_{-1} \\ q^*_0 \\ q^*_1 \\ \vdots \\ q^*_{N-2} \\ q^*_{N-1} \\ q^*_N \end{bmatrix} = \begin{bmatrix} 0 \\ -1 \\ -1 \\ \vdots \\ -1 \\ -1 \\ 0 \end{bmatrix} = \mathcal{B} \tag{C.8}$$

where $a \overset{\text{def}}{=\!=} \dfrac{1}{(ikh/N)^2} = -\left(\dfrac{N}{kh}\right)^2$.

It is, then, readily observed that the non dimensional dynamic pressure can be calculated by inverting the matrix $\mathcal{A}(kh; N)$, thus fully defining the mapping $(kh, N) \mapsto q^*_j \in \mathbb{R}$.

Now, by inserting the eq.(C.2) into eq.(C.4) we obtain:

$$\begin{aligned} &\frac{\partial^2\eta}{\partial t^2} - gh\frac{\partial^2\eta}{\partial x^2} - \frac{h}{N}\frac{\partial^2}{\partial x^2}\sum_{j=0}^{j<N} q_j \Rightarrow \\ \Rightarrow &(ikc)^2 A - gh(ik)^2 A - \frac{h}{N}(ik)^2 gA\sum_{j=0}^{j<N} q^*_j = 0 \Rightarrow \\ \Rightarrow &\frac{c^2}{gh} = 1 + \frac{1}{N}\sum_{j=0}^{j<N} q^*_j = 1 + \overline{(q^*)} \end{aligned} \tag{C.9}$$

Since the dynamic pressure components q^*_j are fully defined, the above equation formulates a dispersion relation of the type $(kh, N) \mapsto c^2/(gh)$.

Bearing that in mind, eq.(C.2) gives:

$$\begin{aligned} &(-ikc)\mathring{u}_j + g(ik)A + (ik)\mathring{q}_j = 0 \Rightarrow \\ \Rightarrow &\mathring{u}_j = \frac{gA}{c}(1 + q^*_j) = \frac{cA/h}{c^2/(gh)}(1 + q^*_j) \Rightarrow \\ \overset{(C.9)}{\Longrightarrow} &h\mathring{u}_j = cA\left(\frac{1 + q^*_j}{1 + \overline{(q^*)}}\right) \end{aligned} \tag{C.10}$$

Bibliography

[1] Kevin A Haas and Ib A Svendsen. Laboratory measurements of the vertical structure of rip currents. *Journal of geophysical research: oceans*, 107(C5):15–1, 2002.

[2] E Laffitte, B Simon, V Rey, J Touboul, and K Belibassakis. Wave-bottom-current interaction, effects of the wave vorticity on the bragg resonance. *Proceedings of the 17th International Maritime Association of the Mediterranean (IMAM2017), Lisbon, Portugal*, pages 9–11, 2017.

[3] Okey G Nwogu. Interaction of finite-amplitude waves with vertically sheared current fields. *Journal of fluid mechanics*, 627:179–213, 2009.

[4] Vincent Rey, Jenna Charland, and Julien Touboul. Wave–current interaction in the presence of a three-dimensional bathymetry: Deep water wave focusing in opposing current conditions. *Physics of Fluids*, 26(9):096601, 2014.

[5] Julien Touboul, Jenna Charland, Vincent Rey, and K Belibassakis. Extended mild-slope equation for surface waves interacting with a vertically sheared current. *Coastal Engineering*, 116:77–88, 2016.

[6] KA Belibassakis, B Simon, Julien Touboul, and V Rey. A coupled-mode model for water wave scattering by vertically sheared currents in variable bathymetry regions. *Wave Motion*, 74:73–92, 2017.

[7] Kostas Belibassakis, Julien Touboul, Elodie Laffitte, and Vincent Rey. A mild-slope system for bragg scattering of water waves by sinusoidal bathymetry in the presence of vertically sheared currents. *Journal of Marine Science and Engineering*, 7(1):9, 2019.

[8] Kostas Belibassakis and Julien Touboul. A nonlinear coupled-mode model for waves propagating in vertically sheared currents in variable bathymetry—collinear waves and currents. *Fluids*, 4(2):61, 2019.

[9] Julien Touboul and Kostas Belibassakis. A novel method for water waves propagating in the presence of vortical mean flows over variable bathymetry. *Journal of Ocean Engineering and Marine Energy*, 5:333–350, 2019.

[10] Pilar García-Navarro, J Murillo, J Fernández-Pato, Isabel Echeverribar, and Mario Morales-Hernández. The shallow water equations and their application to realistic cases. *Environmental Fluid Mechanics*, 19:1235–1252, 2019.

[11] Per A Madsen, Russel Murray, and Ole R Sørensen. A new form of the boussinesq equations with improved linear dispersion characteristics. *Coastal engineering*, 15(4):371–388, 1991.

[12] Per A Madsen, HB Bingham, and HA Schäffer. Boussinesq-type formulations for fully nonlinear and extremely dispersive water waves: derivation and analysis. *Proceedings of the Royal Society of London. Series A: Mathematical, Physical and Engineering Sciences*, 459(2033):1075–1104, 2003.

[13] Philippe Bonneton, Florent Chazel, David Lannes, Fabien Marche, and Marion Tissier. A splitting approach for the fully nonlinear and weakly dispersive green–naghdi model. *Journal of Computational Physics*, 230(4):1479–1498, 2011.

[14] KA Belibassakis and GA Athanassoulis. A coupled-mode system with application to nonlinear water waves propagating in finite water depth and in variable bathymetry regions. *Coastal Engineering*, 58(4):337–350, 2011.

[15] Ch E Papoutsellis, AG Charalampopoulos, and GA Athanassoulis. Implementation of a fully nonlinear hamiltonian coupled-mode theory, and application to solitary wave problems over bathymetry. *European Journal of Mechanics-B/Fluids*, 72:199–224, 2018.

[16] Cyril W Hirt and Billy D Nichols. Volume of fluid (vof) method for the dynamics of free boundaries. *Journal of computational physics*, 39(1):201–225, 1981.

[17] Mark Sussman, Peter Smereka, and Stanley Osher. A level set approach for computing solutions to incompressible two-phase flow. *Journal of Computational physics*, 114(1):146–159, 1994.

[18] Francis H Harlow and J Eddie Welch. Numerical calculation of time-dependent viscous incompressible flow of fluid with free surface. *The physics of fluids*, 8(12):2182–2189, 1965.

[19] M Souli and JP Zolesio. Arbitrary lagrangian–eulerian and free surface methods in fluid mechanics. *Computer methods in applied mechanics and engineering*, 191(3-5):451–466, 2001.

[20] Astrid Decoene and Jean-Frédéric Gerbeau. Sigma transformation and ale formulation for three-dimensional free surface flows. *International Journal for Numerical Methods in Fluids*, 59(4):357–386, 2009.

[21] Norman A Phillips. A coordinate system having some special advantages for numerical forecasting. *J. Meteor.*, 14:184–185, 1957.

[22] Alexandre Joel Chorin. Numerical solution of the navier-stokes equations. *Mathematics of computation*, 22(104):745–762, 1968.

[23] Stephen M Griffies, Claus Böning, Frank O Bryan, Eric P Chassignet, Rüdiger Gerdes, Hiroyasu Hasumi, Anthony Hirst, Anne-Marie Treguier, and David Webb. Developments in ocean climate modelling. *Ocean Modelling*, 2(3-4):123–192, 2000.

[24] Victor P Starr. A quasi-lagrangian system of hydrodynamical equations. *Journal of the Atmospheric Sciences*, 2(4):227–237, 1945.

[25] Kirk Bryan. A numerical method for the study of the circulation of the world ocean. *Journal of computational physics*, 135(2):154–169, 1997.

[26] Ronald C Pacanowski, K Dixon, and Anthony Rosati. The gfdl modular ocean model users guide. *GFDL Ocean Group Tech. Rep*, 2:142, 1991.

[27] Alistair Adcroft, Chris Hill, and John Marshall. Representation of topography by shaved cells in a height coordinate ocean model. *Monthly Weather Review*, 125(9):2293–2315, 1997.

[28] Robert Hallberg and Peter Rhines. Buoyancy-driven circulation in an ocean basin with isopycnals intersecting the sloping boundary. *Journal of Physical Oceanography*, 26(6):913–940, 1996.

[29] Rainer Bleck. Ocean modeling in isopycnic coordinates. *Ocean modeling and parameterization*, pages 423–448, 1998.

[30] Alan F Blumberg and George L Mellor. A description of a three-dimensional coastal ocean circulation model. *Three-dimensional coastal ocean models*, 4:1–16, 1987.

[31] George L Mellor, Tal Ezer, and Lie-Yauw Oey. The pressure gradient conundrum of sigma coordinate ocean models. *Journal of atmospheric and oceanic technology*, 11(4):1126–1134, 1994.

[32] Rainer Bleck. An oceanic general circulation model framed in hybrid isopycnic-cartesian coordinates. *Ocean modelling*, 4(1):55–88, 2002.

[33] Eric P Chassignet, Harley E Hurlburt, Ole Martin Smedstad, George R Halliwell, Patrick J Hogan, Alan J Wallcraft, Remy Baraille, and Rainer Bleck. The hycom (hybrid coordinate ocean model) data assimilative system. *Journal of Marine Systems*, 65(1-4):60–83, 2007.

[34] Alistair Adcroft, Whit Anderson, V Balaji, Chris Blanton, Mitchell Bushuk, Carolina O Dufour, John P Dunne, Stephen M Griffies, Robert Hallberg, Matthew J Harrison, et al. The gfdl global ocean and sea ice model om4. 0: Model description and simulation features. *Journal of Advances in Modeling Earth Systems*, 11(10):3167–3211, 2019.

[35] Matthieu Leclair and Gurvan Madec. z-coordinate, an arbitrary lagrangian–eulerian coordinate separating high and low frequency motions. *Ocean Modelling*, 37(3-4):139–152, 2011.

[36] Mark R Petersen, Douglas W Jacobsen, Todd D Ringler, Matthew W Hecht, and Mathew E Maltrud. Evaluation of the arbitrary lagrangian–eulerian vertical coordinate method in the mpas-ocean model. *Ocean Modelling*, 86:93–113, 2015.

[37] Stephen M Griffies, Alistair Adcroft, and Robert W Hallberg. A primer on the vertical lagrangian-remap method in ocean models based on finite volume generalized vertical coordinates. *Journal of Advances in Modeling Earth Systems*, 12(10):e2019MS001954, 2020.

[38] Xi Chen, Natalia Andronova, Bram Van Leer, Joyce E Penner, John P Boyd, Christiane Jablonowski, and Shian-Jiann Lin. A control-volume model of the compressible euler equations with a vertical lagrangian coordinate. *Monthly Weather Review*, 141(7):2526–2544, 2013.

[39] Iva Kavčič and John Thuburn. A lagrangian vertical coordinate version of the endgame dynamical core. part i: Formulation, remapping strategies, and robustness. *Quarterly Journal of the Royal Meteorological Society*, 144(714):1649–1666, 2018.

[40] Stéphane Popinet. A vertically-lagrangian, non-hydrostatic, multilayer model for multiscale free-surface flows. *Journal of Computational Physics*, 418:109609, 2020.

[41] Alexandre Joel Chorin. A numerical method for solving incompressible viscous flow problems. *Journal of computational physics*, 135(2):118–125, 1997.

[42] Randall J LeVeque. *Finite volume methods for hyperbolic problems*, volume 31. Cambridge university press, 2002.

[43] Emmanuel Audusse. A multilayer saint-venant model: derivation and numerical validation. *Discrete and Continuous Dynamical Systems-B*, 5(2):189–214, 2005.

[44] François Bouchut and Vladimir Zeitlin. A robust well-balanced scheme for multilayer shallow water equations. *Discrete and Continuous Dynamical Systems-Series B*, 13(4):739–758, 2010.

[45] David Lannes and Mei Ming. The kelvin-helmholtz instabilities in two-fluids shallow water models. *Hamiltonian partial differential equations and applications*, pages 185–234, 2015.

[46] Emmanuel Audusse and Marie-Odile Bristeau. Finite-volume solvers for a multilayer saint-venant system. *International Journal of Applied Mathematics and Computer Science*, 17(3):311–320, 2007.

[47] Frédéric Couderc, Arnaud Duran, and J-P Vila. An explicit asymptotic preserving low froude scheme for the multilayer shallow water model with density stratification. *Journal of Computational Physics*, 343:235–270, 2017.

[48] Manuel Castro, Jorge Macías, and Carlos Parés. A q-scheme for a class of systems of coupled conservation laws with source term. application to a two-layer 1-d shallow water system. *ESAIM: Mathematical Modelling and Numerical Analysis*, 35(1):107–127, 2001.

[49] Manuel Jesús Castro-Díaz, Enrique Domingo Fernández-Nieto, José M González-Vida, and Carlos Parés-Madroñal. Numerical treatment of the loss of hyperbolicity of the two-layer shallow-water system. *Journal of Scientific Computing*, 48:16–40, 2011.

[50] François Bouchut and Tomás Morales de Luna. An entropy satisfying scheme for two-layer shallow water equations with uncoupled treatment. *ESAIM: Mathematical Modelling and Numerical Analysis*, 42(4):683–698, 2008.

[51] Eleuterio F Toro. *Riemann solvers and numerical methods for fluid dynamics: a practical introduction*. Springer Science & Business Media, 2013.

[52] Philip L Roe. Approximate riemann solvers, parameter vectors, and difference schemes. *Journal of computational physics*, 43(2):357–372, 1981.

[53] Tuomas Kärnä, Benjamin De Brye, Olivier Gourgue, Jonathan Lambrechts, Richard Comblen, Vincent Legat, and Eric Deleersnijder. A fully implicit wetting–drying method for dg-fem shallow water models, with an application to the scheldt estuary. *Computer Methods in Applied Mechanics and Engineering*, 200(5-8):509–524, 2011.

[54] Gale Dick Van Albada, Bram Van Leer, and WW Roberts Jr. A comparative study of computational methods in cosmic gas dynamics. *Astronomy and Astrophysics, vol. 108, no. 1, Apr. 1982, p. 76-84.*, 108:76–84, 1982.

[55] Ioannis K Nikolos and Argiris I Delis. An unstructured node-centered finite volume scheme for shallow water flows with wet/dry fronts over complex topography. *Computer Methods in Applied Mechanics and Engineering*, 198(47-48):3723–3750, 2009.

[56] Venkat Venkatakrishnan. Convergence to steady state solutions of the euler equations on unstructured grids with limiters. *Journal of computational physics*, 118(1):120–130, 1995.

[57] Manuel J Castro and Carlos Parés. Well-balanced high-order finite volume methods for systems of balance laws. *Journal of Scientific Computing*, 82(2):48, 2020.

[58] Irene Gómez-Bueno, Manuel J Castro, and Carlos Parés. High-order well-balanced methods for systems of balance laws: a control-based approach. *Applied Mathematics and Computation*, 394:125820, 2021.

[59] Alfredo Bermudez and Ma Elena Vazquez. Upwind methods for hyperbolic conservation laws with source terms. *Computers & Fluids*, 23(8):1049–1071, 1994.

[60] Emmanuel Audusse, François Bouchut, Marie-Odile Bristeau, Rupert Klein, and Benoıt Perthame. A fast and stable well-balanced scheme with hydrostatic reconstruction for shallow water flows. *SIAM Journal on Scientific Computing*, 25(6):2050–2065, 2004.

[61] VVe Rusanov. Calculation of interaction of non-steady shock waves withobstacles. *J. Comput. Math. Phys. USSR*, 1:267–279, 1961.

[62] Zhe Liu, Lei Lin, Lian Xie, and Huiwang Gao. Partially implicit finite difference scheme for calculating dynamic pressure in a terrain-following coordinate nonhydrostatic ocean model. *Ocean Modelling*, 106:44–57, 2016.

[63] Guus Stelling and Marcel Zijlema. An accurate and efficient finite-difference algorithm for non-hydrostatic free-surface flow with application to wave propagation. *International journal for numerical methods in fluids*, 43(1):1–23, 2003.

[64] Marcel Zijlema and Guus S Stelling. Further experiences with computing nonhydrostatic free-surface flows involving water waves. *International journal for numerical methods in fluids*, 48(2):169–197, 2005.

[65] Haiyang Cui, JD Pietrzak, and GS Stelling. Optimal dispersion with minimized poisson equations for non-hydrostatic free surface flows. *Ocean Modelling*, 81:1–12, 2014.

[66] TM Shih, CH Tan, and BC Hwang. Effects of grid staggering on numerical schemes. *International Journal for numerical methods in fluids*, 9(2):193–212, 1989.

[67] Akio Arakawa and Vivian R Lamb. Computational design of the basic dynamical processes of the ucla general circulation model. *General circulation models of the atmosphere*, 17(Supplement C):173–265, 1977.

[68] Fang Q Hu. A perfectly matched layer absorbing boundary condition for linearized euler equations with a non-uniform mean flow. *Journal of Computational Physics*, 208(2):469–492, 2005.

[69] Niels G Jacobsen, David R Fuhrman, and Jørgen Fredsøe. A wave generation toolbox for the open-source cfd library: Openfoam®. *International Journal for numerical methods in fluids*, 70(9):1073–1088, 2012.

[70] Hrvoje Jasak, Vuko Vukčević, and Inno Gatin. Numerical simulation of wave loading on static offshore structures. *CFD for wind and tidal offshore turbines*, pages 95–105, 2015.

[71] Maarten W Dingemans. *Water wave propagation over uneven bottoms: Linear wave propagation*, volume 13. World Scientific, 2000.

[72] Simen Å Ellingsen and Yan Li. Approximate dispersion relations for waves on arbitrary shear flows. *Journal of Geophysical Research: Oceans*, 122(12):9889–9905, 2017.

[73] Maarten W Dingemans. Comparison of computations with boussinesq-like models and laboratory measurements. *memo in framework of MAST project (G8-M), Delft Hydraulics memo H1684. 12*, 1994.

[74] Riccardo Fazio and Randall J LeVeque. Moving-mesh methods for one-dimensional hyperbolic problems using clawpack. *Computers & Mathematics with Applications*, 45(1-3):273–298, 2003.

[75] Jihwan Kim and Randall J LeVeque. Two-layer shallow water system and its applications. In *Proceedings of the twelth international conference on hyperbolic problems, Maryland*, volume 52, page 102, 2008.

[76] Marica Pelanti, François Bouchut, and Anne Mangeney. A roe-type scheme for two-phase shallow granular flows over variable topography. *ESAIM: Mathematical Modelling and Numerical Analysis*, 42(5):851–885, 2008.

[77] Andrew L Stewart and Paul J Dellar. Multilayer shallow water equations with complete coriolis force. part 3. hyperbolicity and stability under shear. *Journal of Fluid Mechanics*, 723:289–317, 2013.